

# **Study of spin-reorientation transitions and effect of voltage on magnetic anisotropy**

*A thesis Submitted  
in Partial Fulfilment of the Requirements  
for the Degree of*

**MASTER OF SCIENCE**

*by  
Gaurav Kanu  
under the guidance of  
Professor Subhankar Bedanta*



*to the  
School of Physical Sciences  
National Institute of Science Education and Research  
Bhubaneswar  
15th June 2023*

*Dedicated to my beloved parents & teachers*

## **DECLARATION**

I hereby declare that I am the sole author of this thesis in partial fulfillment of the requirements for a postgraduate degree from National Institute of Science Education and Research (NISER). I authorize NISER to lend this thesis to other institutions or individuals for the purpose of scholarly research.

Gaurav Kanu

Date:

The thesis work reported in the thesis entitled **Study of spin-reorientation transitions and effect of voltage on magnetic anisotropy** was carried out under my supervision, in the School of Physical Sciences at NISER, Bhubaneswar, India.

Signature of the thesis supervisor

School:

Date:

## **ACKNOWLEDGEMENTS**

I want to express my deepest and sincere gratitude to my supervisor Dr Subhankar Bedanta. I am very grateful for his invaluable unwavering guidance, support and encouragement. Sir has always been kind and welcomed my doubts and problems, whether related to the project or not. He has taught me invaluable lessons I will remember and treasure throughout my life.

I thank Mrs Esita Pandey for her never-ending support; Didi helped me from fundamentals to sample preparation, making contacts, measurements, and characterization. I thank Mr Shaktiranjan Mohanty for helping me prepare samples and SQUID measurements. I want to thank Miss Bhuvaneshwari Sharma for helping me with sample preparation and its characterization. I thank Mr Brindaban Ojha for his valuable suggestions and for helping me with sample measurements. I want to thank Mr Abhishek Mishra and Ms Swayangpriya Mahanta for helping me with the experiments.

I would like to thank all Laboratory for Nanomagnetism and Magnetic Materials (LNMM) members for their constant encouragement, motivation, and support, due to which this project could be completed within the expected time duration.

I wish to thank all my professors for taking the courses and labs, always welcoming my silliest questions with open hearts, and helping me whenever needed. I would like to acknowledge the support of the National Institute of Science Education and Research (NISER) for providing all the instrumental facilities for project completion.

I wish to thank all my closest friends, Santosh, Tamoghna, Dinesh, Varun, Gautameshwar, Prasanjit and my childhood friends Abhishek, Shubham and Shivani for always being there and helping me in difficult times and making my master's journey beautiful and amazing.

Last but not least, I would like to thank my parents for their blessings, love, care,

and motivation helped me in every aspect of my life. I would like to thank my elder brother Kundan for his continuous support and encouragement, because of which I was always able to stay motivated toward my work.

During my five-year adventure at NISER Bhuvaneshwar, I met many people and made friends. Mentioning their names here is difficult, but I am always grateful to you for the lessons you taught, the friendship, and the time we enjoyed together.

## ABSTRACT

Tuning magnetic anisotropy of materials has emerged as a crucial aspect of developing advanced magnetic devices with enhanced performance and novel functionalities. This thesis highlights the significance of tuning magnetic anisotropy through thickness and voltage control, showcasing its potential in manipulating magnetic properties and enabling technological breakthroughs. By varying the thickness of ferromagnetic layers and applying voltage-induced effects, researchers can precisely control the preferred orientation of magnetic moments, leading to improved data storage, efficient energy consumption, and exploration of new functionalities in spintronic and magneto-electric devices. Proximity to the spin reorientation transition (SRT) has been found to be particularly advantageous for studying magnetic skyrmions, topologically stable whirlpool-like structures, and understanding their behaviour and dynamics. Here we report a systematic thickness-dependent study on Pd/Co/Cu system. We observed that with increasing thickness of the FM layer, magnetization shifts from perpendicular to the in-plane direction. From calculations, we found the SRT of Co lies near 0.70 nm. Later, we performed voltage-controlled measurements on Pt/Co/Pt system and marked the shift in magnetization reversal, which was observed as reversible by applying the opposite voltage. The magnitude of the shift in coercivity is marked as 5.04% and 3.52% for Co 0.8 nm and 1.3 nm.

# Contents

<b>1</b>	<b>Introduction</b>	<b>1</b>
1.1	Magnetic anisotropy . . . . .	4
1.1.1	Surface anisotropy . . . . .	6
1.1.2	Perpendicular magnetic anisotropy (PMA) . . . . .	7
1.1.3	Interfacial perpendicular magnetic anisotropy . . . . .	7
1.1.4	Spin Reorientation transitions (SRT) . . . . .	9
1.2	Voltage controlled magnetism . . . . .	10
1.2.1	Carrier modulation . . . . .	11
1.2.2	Strain effect . . . . .	12
1.2.3	Exchange coupling . . . . .	13
1.2.4	Orbital reconstruction . . . . .	13
1.2.5	Electrochemical effect . . . . .	14
<b>2</b>	<b>Experimental Techniques</b>	<b>15</b>
2.1	Sputtering . . . . .	15
2.1.1	DC Sputtering . . . . .	15
2.1.2	RF sputtering . . . . .	16
2.2	X-Ray reflectometry (XRR) . . . . .	17
2.3	X-ray diffraction (XRD) . . . . .	18
2.4	Magneto optic Kerr-effect . . . . .	20
2.5	Superconducting Quantum Interference Device (SQUID) . . . . .	21
<b>3</b>	<b>Spin reorientation transition of Co in Pd/Co/Cu ultra-thin films.</b>	<b>23</b>
3.1	Sample preparation . . . . .	23
3.2	Structural characterization . . . . .	24
3.2.1	XRR analysis . . . . .	25
3.3	Study of magnetization reversal and effective anisotropy . . . . .	25
<b>4</b>	<b>Voltage-controlled magnetic anisotropy in perpendicularly magnetized Pt/Co/Pt ultrathin films</b>	<b>37</b>
4.1	Sample preparation . . . . .	37
4.2	VCMA measurement . . . . .	39
4.3	Structural characterization . . . . .	40

---

*CONTENTS*

4.3.1 XRR analysis . . . . .	40
4.4 Magnetic characterization . . . . .	41
4.4.1 Magnetization reversal with voltage application . . . . .	42
<b>5 Summary and Conclusions</b>	<b>50</b>
<b>References</b>	<b>57</b>

# List of Figures

1.1	Reported writing energy for toggle (MRAM) (red dots) and (STT-MRAM) (blue dots) as a function of magnetic tunnel junctions (MTJ) cell size and the target area for voltage-torque MRAM.[1]	3
1.2	Schematic magnetization curves for a ferromagnet with the field oriented along the hard and easy directions[2].	4
1.3	Easy, medium, and hard directions of magnetization in a unit cell of BCC iron[2].	5
1.4	Polar and longitudinal MOKE loops measured across the range of the SRT for successive Fe thickness between 3.0 and 2.0 ML for Fe/Au(001). The hard-axis loops are given together with the corresponding simulated curves.[3], [4]	10
2.1	Schematic diagram for magnetron sputtering system . . . . .	16
2.2	(a) An image of a multipurpose high vacuum deposition system manufactured by MANTIS at NISER Bhubaneswar. (b) A schematic representation of the deposition geometry of the system. . . . .	17
2.3	Schematic for X-ray reflectivity technique, the incident X-rays get reflected from the sample surface. The plot at the lower left shows when $\omega < \theta_c$ , middle one shows when $\omega = \theta_c$ and right shows when $\omega > \theta_c$ .	18
2.4	Schematic of a typical X-ray reflectivity profile. [5] . . . . .	19
2.5	The schematic diagrams of (a) polar, (b) longitudinal, and (c) transverse MOKE. . . . .	20
2.6	Pick-up-coil geometry and theoretical response signal of an ideal dipole vs scan length in an MPMS SQUID magnetometer. [6] . . . . .	22
3.1	Schematic of sample structure. . . . .	24
3.2	XRR fits of sample <b>S1</b> and <b>S2</b> . . . . .	25
3.3	Polar MOKE measurement of the samples, where <b>S1</b> and <b>S2</b> have polar configuration as easy axis . . . . .	26
3.4	Kerr-microscopy images of <b>S1</b> and <b>S2</b> in polar MOKE geometry. Observed bubble domains around the coercivity (image (c)) . . . . .	27
3.5	Samples <b>S3</b> , <b>S4</b> and <b>S5</b> have hard axis as the polar configuration. The magnetization curve didn't saturate. . . . .	28
3.6	Longitudinal MOKE measurement of the samples, the sample didn't saturate due to the instrumental constraint of a higher magnetic field.	29
3.7	Sample mounted inside a straw for out-of-plane measurements. . . . .	30

---

*LIST OF FIGURES*

---

3.8	Magnetization reversal measured by SQUID-VSM (a) <b>S1</b> , (b) <b>S2</b> , (c) <b>S3</b> , (d) <b>S4</b> , (e) <b>S5</b> , where the magnetic field was applied perpendicular to the film at room temperature. . . . .	31
3.9	Sample mounted on quartz glass for in-plane measurement in SQUID magnetometry. . . . .	32
3.10	Magnetization reversal measured by SQUID-VSM (a) <b>S1</b> , (b) <b>S2</b> , (c) <b>S3</b> , (d) <b>S4</b> , (e) <b>S5</b> , where the magnetic field was applied in-plane to the film at room temperature. . . . .	33
3.11	Calculation of effective anisotropy ( $K_{\text{eff}}$ ). . . . .	35
3.12	$t.K_{\text{eff}}$ vs $t$ plot, SRT for Cobalt is observed around 0.70 nm. . . . .	35
3.13	Total anisotropy energy $K_u$ multiplied by the bilayer period A vs the Co layer thickness $t$ . Symbols denote experimental data for different Pd thicknesses. The solid line is linear fit . . . . .	36
4.1	Edge-covered substrate before deposition. . . . .	38
4.2	Schematic of sample structure . . . . .	39
4.3	The VCMA setup . . . . .	40
4.4	XRR fit of sample <b>S<sub>1</sub></b> . . . . .	41
4.5	Schematic of <b>S<sub>1</sub></b> with applied bias voltage. . . . .	42
4.6	Magnetic hysteresis loop measure by polar MOKE microscopy of <b>S<sub>1</sub></b> with varying voltage. . . . .	43
4.7	Zoomed Fig 4.6 to observe the change in coercivity with voltage. . . . .	44
4.8	<b>S<sub>1</sub></b> magnetic domain images at the coercivity at respective voltages. . . . .	45
4.9	Schematic of <b>S<sub>2</sub></b> with applied bias voltage. . . . .	46
4.10	Magnetic hysteresis loop measured by polar MOKE microscopy of <b>S<sub>2</sub></b> with varying voltage. . . . .	47
4.11	Zoomed Fig 4.10 to observe the change in coercivity with voltage. . . . .	48
4.12	<b>S<sub>2</sub></b> magnetic domain images at the coercivity at respective voltages. . . . .	49

# List of Tables

3.1	Sample name and structure . . . . .	24
4.1	<b>S<sub>1</sub></b> XRR fit parameters. . . . .	41
4.2	Coercive field values at the respective voltage for sample S <sub>1</sub> . . . . .	43
4.3	Coercive field values at the respective voltage for sample S <sub>2</sub> . . . . .	47

# Chapter 1

## Introduction

Tuning magnetic anisotropy through thickness and voltage effects has emerged as a significant area of research in recent years, driven by the need to enhance the performance of magnetic devices and explore novel functionalities. Magnetic anisotropy refers to the preferred orientation of magnetic moments within a material, which determines its response to external magnetic fields. By manipulating the anisotropy, researchers can control various magnetic properties, such as the stability of magnetic domains, the switching behaviour of magnetic elements, and the efficiency of data storage and processing.

Modulation of magnetic anisotropy through sample thickness not only allows change in the direction of spontaneous magnetization in a ferromagnet (from out-of-plane to in-plane) but also helps in the nucleation of chiral structures such as magnetic skyrmions when in proximity to spin reorientation transition (SRT). Skyrmions are topologically protected chiral structures, and their size ranges in sub nanometers. Due to their small size and dynamics, magnetic skyrmions can be a potential candidate for data transfer applications (skyrmion racetrack memories [7], [8]).

Tuning magnetic anisotropy via an external electric field is known as Voltage-controlled magnetic anisotropy (VCMA). It is a fascinating phenomenon that has garnered significant attention from researchers in recent years. The origins of VCMA can be traced back to the discovery of the magnetostriction effect, which was first observed by James Joule in 1842. Magnetostriction refers to the change in the di-

mensions of a material in response to a magnetic field. The change in the material's dimension causes strain, which modifies the anisotropy of the materials, which in turn can affect its response to an external electric field. The development of MRAM holds immense potential to serve as a high-speed, nonvolatile memory with excellent write endurance and compatibility with CMOS technology, making it ideal for both standalone and embedded memory applications. Nevertheless, one primary obstacle to overcome is minimizing the energy required to switch the magnetization, i.e., to write information [1].

The first experimental evidence of voltage control of magnetic anisotropy in ferromagnets at room temperature was reported by Weisheit et al. in 2007 [9]. They observed a change in the coercivity up to -4.5% in FePt and 1% in FePd films with an applied external voltage. The samples were dipped in Propylene Carbonate (electrolyte), and an electrolytic double layer was formed at the sample surface, generating a large electric field. It has been understood that the electric field modifies the magneto-crystalline anisotropy energy (MAE)[10, 11, 12]

Since then, significant progress has been made in developing VCMA materials and devices, with numerous applications being explored in data storage and spintronics areas. STT-MRAMs have high writing energy ( $\sim 100fJ/bit$ ) comparatively to normal MRAMs but have significantly higher storage density, as shown in Figure 1.1. Therefore, developing a novel type of memory with low operating and standby energy can greatly impact the design of future memory hierarchy [1]. VCMA effect could play an important role in making energy-efficient non-volatile memory devices and has the potential to play a pivotal role in shaping the future of information technology and materials science.

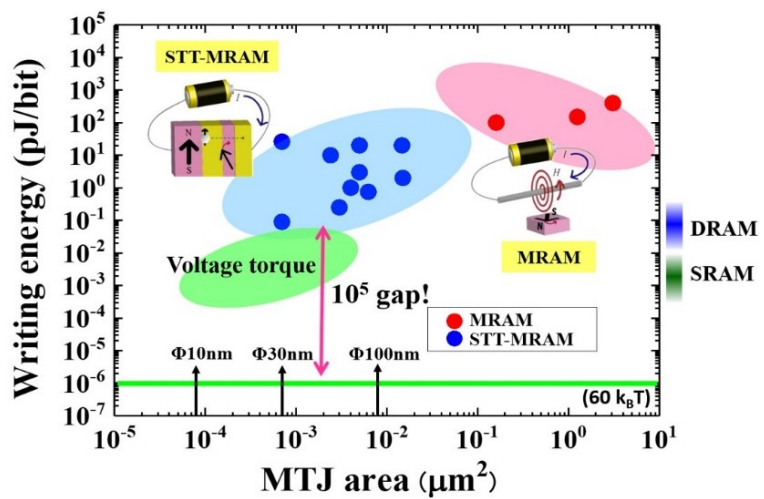


**Figure 1.1:** Reported writing energy for toggle (MRAM) (red dots) and (STT-MRAM) (blue dots) as a function of magnetic tunnel junctions (MTJ) cell size and the target area for voltage-torque MRAM.[1]

# Theoretical background

## 1.1 Magnetic anisotropy

The magnetization in ferromagnetic crystals tends to align along certain preferred crystallographic directions. The preferred directions are called the “easy” axes since it is easiest to magnetize a demagnetized sample to saturation if the external field is applied along a preferred direction. Figure 1.2 shows the amount of external field required to reach saturation magnetization along the easy and hard axis.

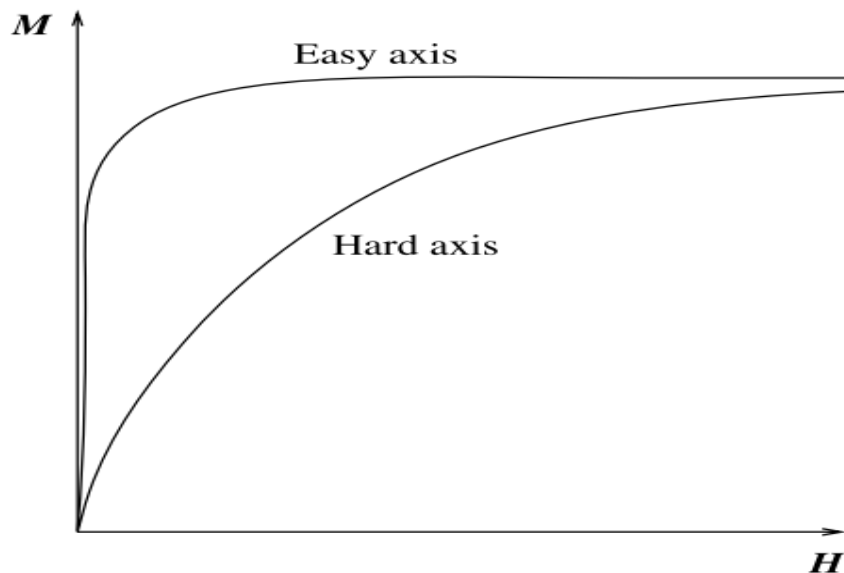


**Figure 1.2:** Schematic magnetization curves for a ferromagnet with the field oriented along the hard and easy directions[2].

In both the cases saturation magnetization is achieved but much larger applied field is required to reach saturation along the hard axis than along the easy axis.

**Uniaxial crystal:**

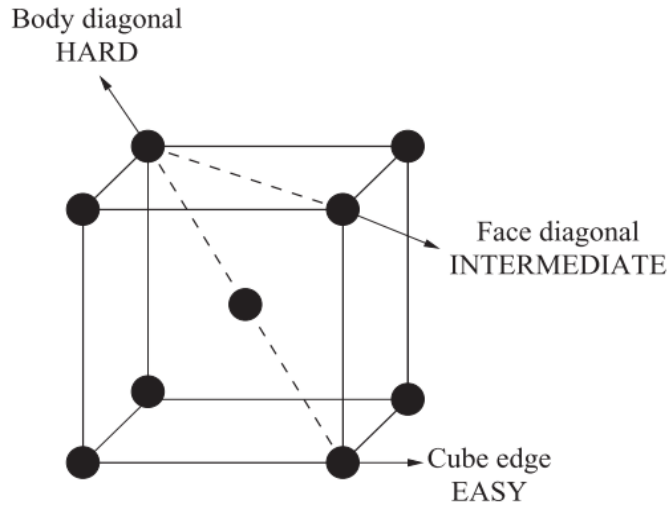


**Figure 1.3:** Easy, medium, and hard directions of magnetization in a unit cell of BCC iron[2].

In a uniaxial crystal, there exists only a single easy axis along which the magnetization reversal is fastest. The anisotropy energy is given as:

$$E_a = K_u \sin^2 \theta \quad (1.1)$$

Where  $E_a$  is the anisotropy energy density,  $\theta$  is the angle between the magnetization and the easy axis, and  $K_u$  are the anisotropy constants.  $E_a$  is a minimum when  $M_s$  is in that direction.

When  $K_u$  is positive, energy is minimum at  $\theta = 0$ , which is the axis of easy magnetization.

The energy costs to turn the magnetization from the direction of easy axis into any other direction. In the framework of micromagnetics, the average energy density of the uniaxial magnetic anisotropy is given by:

$$E_{ani} = -\mathbf{K}(\mathbf{m} \cdot \mathbf{n})^2 \quad (1.2)$$

where  $\mathbf{K}$  is the anisotropy constant, and  $\mathbf{n}$  is the direction.

### Cubic crystal:

$$E_a = K_0 + K_1(\alpha_1^2\alpha_2^2 + \alpha_2^2\alpha_3^2 + \alpha_3^2\alpha_1^2) + K_2(\alpha_1^2\alpha_2^2\alpha_3^2) \quad (1.3)$$

where  $\alpha_1, \alpha_2, \alpha_3$  are the direction cosines,  $\alpha_i = \cos \theta_i$  and  $\theta_i$  are the angles between the magnetization and the easy axes.

$K_0, K_1, K_2$  are anisotropy constants. For a particular material at a particular temperature the anisotropy constants are expressed in erg/cm<sup>3</sup> (cgs) or J/m<sup>3</sup> (SI).

#### 1.1.1 Surface anisotropy

In an isotropic medium surface, anisotropy can be expressed by [13]:

$$E_s = K_s[1 - (\vec{M} \cdot \vec{n})^2] \quad (1.4)$$

where  $\vec{M}$  is the magnetization vector and  $\vec{n}$  is the normal to the surface. For the positive value of  $K_s$ , the surface energy density  $E_s$  is minimum when the magnetization is perpendicular to the surface. They become important for very thin films since the effective anisotropy of a thin film system is given by:

$$K_{eff} = K_V + 2K_S/t \quad (1.5)$$

where  $t$  is the thickness of the ferromagnetic layer,  $K_V$  and  $K_S$  are the volume and surface anisotropies respectively. At  $t = t_c$ (critical thickness),  $K_{eff}$  goes to zero; therefore the critical thickness can be given as:

$$t_c = -2K_S/K_V \quad (1.6)$$

At critical thickness, the surface and volume contributions become equal. So when  $t > t_c$ , the system shows in-plane magnetic anisotropy; otherwise, the system shows out-of-plane magnetic anisotropy.

### 1.1.2 Perpendicular magnetic anisotropy (PMA)

For a thick ferromagnetic film the equilibrium magnetization aligns in the plane, primarily due to the demagnetization field. The magnetic energy is lowered when the magnetization direction is in-plane rather than perpendicular-to-plane due to the demagnetization field. However, electrons at the interface may experience additional magnetic energy owing to the spin-orbit interaction. This energy contribution can be significant and reduces the overall magnetic energy in the perpendicular-to-plane direction. As a result, the equilibrium magnetization aligns perpendicularly to the plane, an effect referred to as perpendicular magnetic anisotropy (PMA).

The strength of the spin-orbit interaction and hence the PMA intensifies only when the electron orbitals become asymmetric or deformed in a particular direction. The interfacial PMA arises when the orbital deformation results from breaking periodicity at an interface, whereas the bulk PMA occurs due to crystal spatial asymmetry.

### 1.1.3 Interfacial perpendicular magnetic anisotropy

Interfacial perpendicular magnetic anisotropy (PMA) arises from the interaction between the magnetic moments of atoms or ions in two adjacent materials across an interface, which causes the magnetic moments to align perpendicular to the interface preferentially. This phenomenon has become a topic of great interest in recent years

due to its potential for applications in magnetic data storage and spintronics. The origin of interfacial PMA can be attributed to the presence of an interfacial layer with a different crystal structure, composition, or bonding [14]. The specific mechanisms that lead to PMA can vary depending on the materials involved, but in general, they involve competition between different types of magnetic interactions that are influenced by the interfacial structure and composition. One important mechanism for interfacial PMA is the interfacial orbital moment effect, which arises from a coupling between the spin and orbital moments of the atoms or ions at the interface. This can lead to a perpendicular magnetic anisotropy by inducing a symmetry-breaking effect that favours the alignment of the magnetic moments perpendicular to the interface.

### **Interface orbital moment**

Interface orbital moment refers to the magnetic moment that arises due to the spin-orbit interaction at the interface between two materials with different electronic structures. The spin-orbit interaction is a relativistic effect that arises from the interaction between the magnetic field generated by the electron's motion and the electron's intrinsic spin.

At an interface between two materials, such as a metal and an insulator [14, 15, 16], the electron's motion can become confined, leading to a change in its electronic structure and hence its spin-orbit interaction. This change in spin-orbit interaction can result in the emergence of an interface orbital moment, which contributes to the overall magnetization of the interface.

### 1.1.4 Spin Reorientation transitions (SRT)

A spin reorientation transition (SRT) is, generally, a cross-over between different states of macroscopic magnetic order (antiferromagnetic, canted, ferrimagnetic or ferromagnetic), which is effected through a rotation of the macroscopic magnetization into a new equilibrium direction under variation of experimentally controllable, or at least identifiable, parameters such as temperature, stress, film thickness, etc. [4]. Such variations cause a change in contributions from magnetic anisotropy, which in turn leads to a change in the energetically preferred axis of magnetization, i.e. easy axis.

Upon increase of the film thickness, the magnetic easy axis of the system would rotate away from  $\mathbf{n}$  (normal to the surface) and would end up in the film to minimize the demagnetizing energy[4].

The reorientation process has its many use in applications such as perpendicular magnetic recording where there is a significant increase in area density as compared to in-plane recording.

The spin reorientation transitions can take place via 2 ways:

1. Canted state of magnetization with a thickness-dependent variation of the canting angle.
2. Coexisting state, in which  $\mathbf{M}$  (magnetization) may be oriented partially perpendicularly and partially in the plane, raising the question of possible domain formation and evolution.

Fig.1.4 shows MOKE hysteresis loops in polar and longitudinal geometries, the

transition from the in-plane orientation of  $\mathbf{M}$  to out-of-plane with varying thickness of Fe in Fe/Au thin film. The hysteresis loop marks the transition occurring at 2.0 monolayer (ML) thickness of Fe.

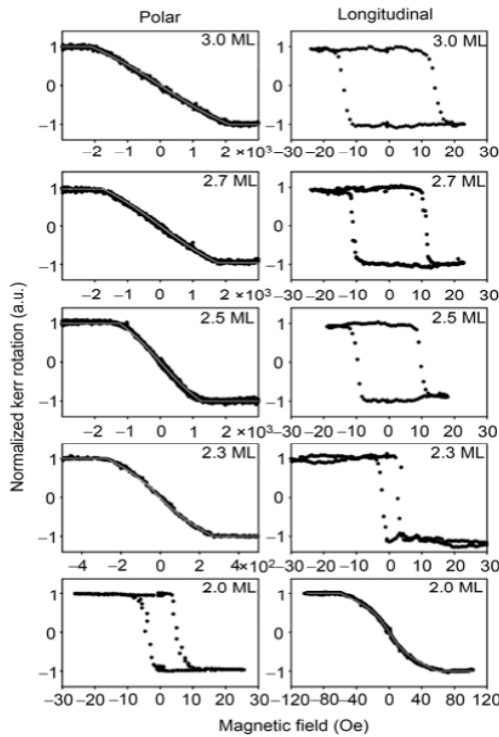


**Figure 1.4:** Polar and longitudinal MOKE loops measured across the range of the SRT for successive Fe thickness between 3.0 and 2.0 ML for Fe/Au(001). The hard-axis loops are given together with the corresponding simulated curves.[3], [4]

## 1.2 Voltage controlled magnetism

Over the years, researchers have found that through voltage application, exciting properties of ferromagnets, such as Curie temperature [17, 18], exchange bias [19] and magnetocrystalline anisotropy energy (MAE) [10] can be modified or tuned. Some materials with multiple ferroic properties can be of great use for application-based devices as they show both ferroelectric and ferromagnetic properties. These

materials respond to an electric field which modifies the spin-orbit coupling, thus the magnetic anisotropy energy, leading to a VCMA effect [20].

In storage and memory devices, the magnetic anisotropy of the material plays a vital role; thus, modification of anisotropy through electric fields has gained popularity over time due to lower power consumption.

In the junction between an ultrathin ferromagnet and a non-magnetic insulator, the magnetic anisotropy of the ferromagnet changes when an external electric field is applied through the insulator. This phenomenon is known as the voltage-controlled magnetic anisotropy (VCMA) effect [21]. The first observation of VCMA in 3d transition metal was done in a liquid electrolyte in room temperature, overtime researchers demonstrated VCMA in ultra-thin 3d transition metals using all solid structures. [10, 22, 23, 24]

There are different mechanisms through which the anisotropy of the magnetic material gets modulated on the application of the electric field. Carrier modulation, strain effect, exchange coupling, orbital reconstruction, and electrochemical effect are some of those mechanisms; discussed as follows:

### **1.2.1 Carrier modulation**

The magnetic properties of a ferromagnetic material can experience a significant alteration if there is a change in the carrier density of the system. The carrier density can be easily controlled by applying an electric field, thus making it possible to modulate the material's magnetic properties. However, metallic materials exhibit a strong screening effect towards electric fields, necessitating the application of a large electric field to alter their carrier density. It is advisable to use ultra-thin metallic

systems with a high surface-to-volume ratio to achieve a significant change in magnetic properties.

Metals contain unpaired *d* electrons, which have energies close to the Fermi energy and act as the free charge carriers of the metal, controlling its magnetic properties. Any alteration in the density of these electrons leads to a direct change in the magnetocrystalline anisotropy of the material, owing to the modification of the number of 3d electrons [25]. The application of an electric field can modify the energy and electron occupancy of the  $3d_{z^2}$  orbital, leading to a change in the magnetic anisotropy of the material. Furthermore, the electric field can shift the Fermi level, thereby affecting the relative electron occupancy and hence the magnetic anisotropy of the material. However, the small screening thickness of the metallic system means that the carrier modulation mechanism plays only a minor role in the voltage control of ferromagnetic metals.

### **1.2.2 Strain effect**

The magnetic properties of ferromagnetic materials can be easily manipulated by applying strain to the sample. It is commonly believed that there will be a significant alteration in the magnetic properties of the ferromagnetic layer due to the transfer of strain from the ferroelectric (FE) layer to the ferromagnetic layer [26]. On application of an electric field, the shape of the FE layer undergoes significant deformation due to the inverse piezoelectric effect, leading to strain on the adjacent ferromagnetic layer and modulation of its magnetic properties. This mechanism is much more effective than carrier modulation because it is not limited by screening effects.

The transfer of strain between the FE and ferromagnetic layers results in a change in the magnetocrystalline anisotropy of the ferromagnetic layer, which can be easily

controlled by varying the strength of the applied electric field. Moreover, this technique does not require any alteration in the carrier density of the system, making it suitable for applications where carrier modulation is not feasible or effective.

### 1.2.3 Exchange coupling

The modulation of magnetism in ferromagnetic systems can also be governed by the exchange coupling mechanism. The interface between ferromagnets and antiferromagnets exhibits the exchange coupling or exchange bias (EB) effect, which results in a shift in the hysteresis curve. Single-phase multiferroic materials, such as  $Cr_2O_3$  [27, 19], have a higher preference as these materials exhibit both ferroelectric and ferromagnetic properties within a single crystallographic phase on the application of electric fields. Then, due to the exchange coupling effect, the magnetic properties of adjacent ferromagnetic layers will be modulated when the magnetic properties of the multiferroic layer are modulated.

### 1.2.4 Orbital reconstruction

The interplay of orbitals in a ferromagnetic material is a critical factor in manipulating its magnetic properties. The alteration of the orbital configuration of the material through electron transfer between atoms leads to changes in the anisotropy of the sample. At the interface of a metal and oxide, there is a phenomenon of orbital hybridization, which causes reconstruction of the atomic orbitals [24]. When an electric field is applied to the sample, the distribution of electrons shifts from one atom to another, leading to transformations in the physical characteristics of the metal.

### 1.2.5 Electrochemical effect

Systems containing ionic liquid or materials with high oxygen mobility such as GdO<sub>x</sub> exhibit modulations in magnetic properties upon application of an electric field due to redox reactions [28]. Under the influence of an electric field, the ions in the ionic liquid are separated and migrate to opposing sides of the magnetic sample, creating an electric double layer (EDL) at the interface [29]. The EDL generates an extremely high electric field, as the separation between both layers is negligible and may induce the migration of oxygen atoms into the ferromagnetic sample, leading to alterations in its magnetic properties. In a recent publication by C.Wang et al. [30], they prepared an ionic gel by mixing a polymer with an ionic liquid. Due to the flexible nature of the ionic gel, it could be bent and can be pasted on the magnetic sample.

# Chapter 2

## Experimental Techniques

### 2.1 Sputtering

Sputtering is a process of ejecting atoms or ions from the surface of a solid material by bombarding it with high-energy particles, such as ions or neutral atoms. When these high-energy particles collide with the surface of the solid material, they transfer energy to the surface atoms, causing some of them to be ejected or sputtered out.

#### 2.1.1 DC Sputtering

DC sputtering is a physical vapour deposition technique that deposits various materials' thin films onto a substrate. In this process, a high-energy DC voltage is applied to a target material, typically made of the material to be deposited. At the same time, a low-pressure gas, such as argon (as in our sputtering system), is introduced into the vacuum chamber. The free electrons from the plasma surface collide with the argon atoms, forming Ar<sup>+</sup> ions. These Ar<sup>+</sup> ions get attracted towards the negatively charged target, which thus leads to the removal of target material due to momentum transfer. The ejected target material gets deposited on the substrate, which is kept along the propagation path.

The sputtering process can be enhanced by placing an annular permanent magnet below the target (i.e. cathode) with another magnet of opposite polarity placed co-axially inside the annular magnet, as shown in Figure 2.1. The co-axially placed

magnets trap the free electrons in the close vicinity of the target, and this helps to overcome the chances of the free electron hitting/ bombarding the depositing substrate; thus, this leads to a higher sputtering rate and a higher degree of ionization, resulting in a denser and more uniform film; this process is known as "magnetron sputtering".[31]

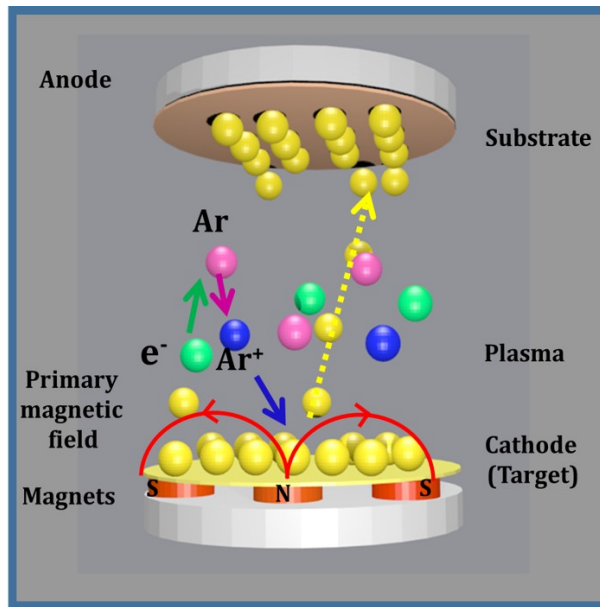


**Figure 2.1:** Schematic diagram for magnetron sputtering system

DC sputtering has certain drawbacks, such as only conducting materials can be deposited through it, and using insulators causes the extinguishment of plasma as gas ionisation requires free electrons. By definition, insulators do not have free electrons, making plasma generation difficult.

### 2.1.2 RF sputtering

Radio Frequency (RF) sputtering is widely used to deposit insulating materials. Here alternating RF powering is applied where during the first half cycle (negative half), Ar<sup>+</sup> ions get attracted towards the target, causing charge accumulation. In the next

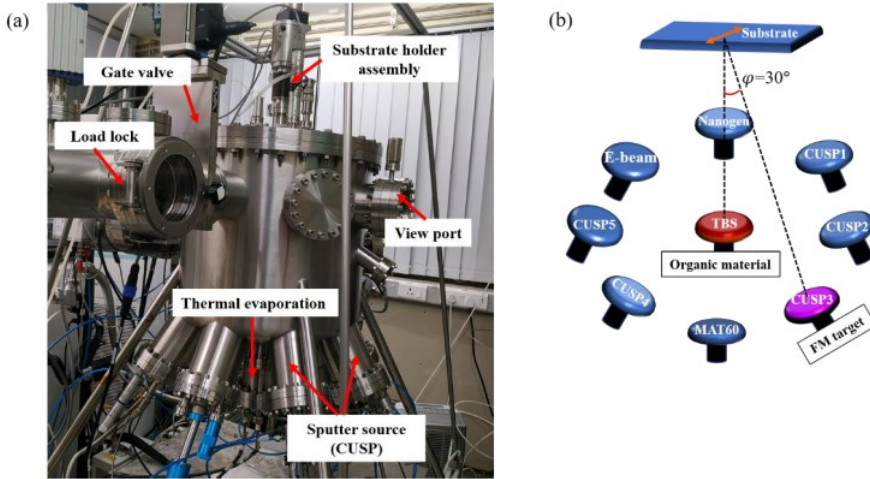


**Figure 2.2:** (a) An image of a multipurpose high vacuum deposition system manufactured by MANTIS at NISER Bhubaneswar. (b) A schematic representation of the deposition geometry of the system.

half cycle (positive half), electrons get attracted towards the target, causing charge neutralization. The deposition rate in RF sputtering is significantly less than in DC sputtering, as only during negative half-cycle sputtering occurs.

## 2.2 X-Ray reflectometry (XRR)

X-ray reflectometry (XRR) is one of the powerful tools used to determine the thickness, density and roughness of single-layer and multilayer samples. XRR analysis can be performed on both crystalline and amorphous materials. Total reflection occurs when X-rays are applied at a lower angle (at or below the critical angle  $\theta_c$ ). The higher the incident angle, the critical angle deeper the X-rays get transmitted into the sample, as shown in Figure 2.3.

Every material has its own critical angle. The critical angle is determined by the angle at which the intensity drops. The reflected X-rays will either constructively or destructively interfere with each other depending upon if this material, serving as a

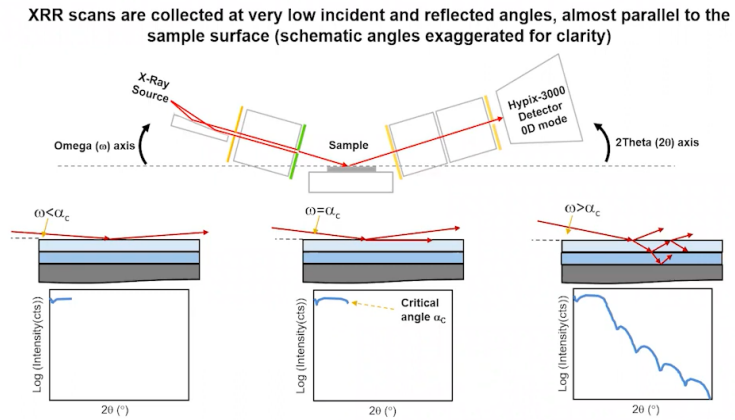


**Figure 2.3:** Schematic for X-ray reflectivity technique, the incident X-rays get reflected from the sample surface. The plot at the lower left shows when  $\omega < \theta_c$ , middle one shows when  $\omega = \theta_c$  and right shows when  $\omega > \theta_c$

substrate, is evenly overlaid with another material with a different electronic density. The interference-induced oscillation pattern resulted from both reflected X-rays from the interface between the substrate and the thin film and the free surface of the thin film. The intensity scattered by a sample is proportional to the square of the modulus of the Fourier transform of the electron density. The film thickness is determined from the periodicity of the oscillation and information on the surface and interface from the angular dependency of the oscillation pattern's amplitude.

## 2.3 X-ray diffraction (XRD)

In materials science and engineering, X-ray diffraction (XRD) is a frequently used analytical technique for studying the structure and properties of crystalline materials. The method is based on Bragg's law, which states that X-rays interacting with a crystal lattice will diffract at specific angles depending on the lattice spacing and orientation.

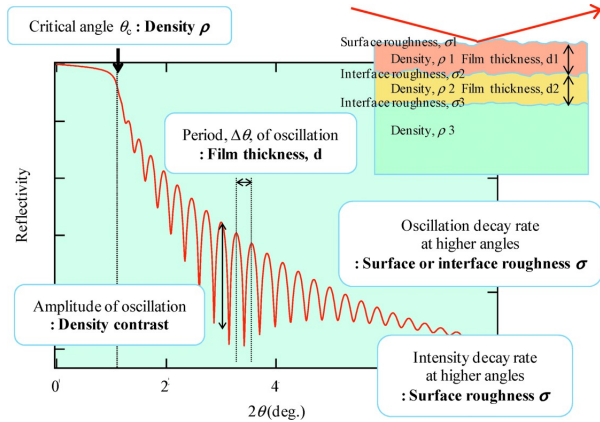


**Figure 2.4:** Schematic of a typical X-ray reflectivity profile. [5]

The idea of diffraction describes how waves bend around actual objects. Whether measured in kilometres or angstroms, this can be used on any scale. The Angstrom scale is used in this investigation. X-rays can diffract among a mineral sample's atoms when focused on it. The distance between atoms may cause a specific angle to be diffracted. Bragg's law takes advantage of this idea.

The equation for diffraction is given by

$$2ds\sin(\theta) = n\lambda \quad (2.1)$$

Where  $\lambda$  is the wavelength of the X-ray,  $d$  = lattice spacing of the diffracting planes,  $\theta$  = the angle between the X-ray beam and the diffraction planes, and  $n$  is the integer index. The following equations for different lattice groups can calculate lattice parameters:

$$\text{Cubic} : \frac{1}{d^2} = \frac{(h^2 + k^2 + l^2)}{a^2} \quad (2.2)$$

$$\text{Hexagonal} : \frac{1}{d^2} = \frac{4(h^2 + hk + k^2)}{a^2} + \frac{l^2}{c^2} \quad (2.3)$$

The  $0 - 2\theta$  scanning mode and the grazing scanning mode have been used the most frequently to gather information on the thin film structure out of all the different X-ray diffraction scanning modes. The rocking curve mode is frequently used in addition to these two scanning modes to assess texture quality. Off-spectral scans are used to examine the epitaxial connection between the substrate underlayer and the top layer and the texture quality.

## 2.4 Magneto optic Kerr-effect

When linearly polarised light reflects from a ferromagnetic sample placed in the external magnetic field, there is rotation in the plane of polarisation of light, due to which linearly polarised light becomes elliptically polarised. This is known as the magneto-optical Kerr effect (MOKE) [32].

The Kerr rotation ( $\theta_k$ ) and ellipticity ( $\epsilon_k$ ) are related to each other by a relation:  
 $\theta_k + i\epsilon_k = k/r$ , in the limit  $k \ll r$ .

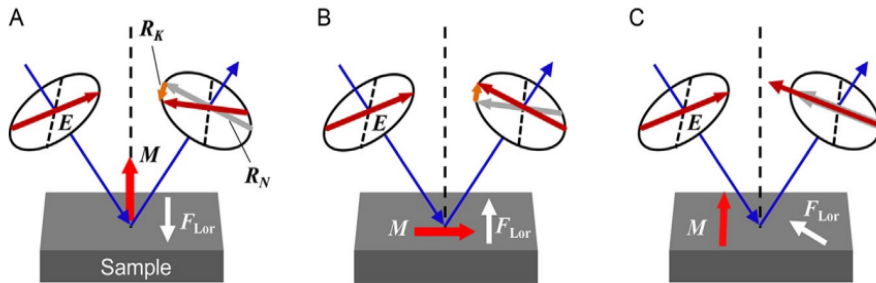


**Figure 2.5:** The schematic diagrams of (a) polar, (b) longitudinal, and (c) transverse MOKE.

Depending upon the direction of the magnetization vector ( $\vec{M}$ ) and the plane of incidence of light, the geometries can be classified into three types Polar, Longitudinal and Transverse, as shown in Figure 2.5.

1. Polar: In polar geometry, the magnetization vector is perpendicular to the sample surface and parallel to the plane of incidence of the light.
2. Longitudinal: In longitudinal geometry, the magnetization vector is parallel to the sample surface and the plane of incidence of light.
3. Transverse: In Transverse geometry, the magnetization vector is parallel to the sample surface and perpendicular to the plane of incidence. Figure 2.5 shows all the MOKE geometries.

## 2.5 Superconducting Quantum Interference Device (SQUID)

SQUID (Superconducting Quantum Interference Device) magnetometer is based on the tunnelling of superconducting electrons across two parallel, very narrow insulating gaps, called a Josephson junction, between two superconductors. It measures magnetic properties such as magnetic moment with high sensitivity. The changes in a magnetic field to the level of one flux quantum can be sensed by the SQUID. Based on the flux quantization principle, the flux enclosed by the superconducting loop is quantized in units of  $2.067 \times 10^{-15} T.m^2$ .

The vibration of the magnetic sample produces an alternating magnetic flux which links with the pick-up coil, the flux current produced in the coil is inductively transferred to the coupled SQUID. In response, there is a proportional output voltage based on the influence of magnetic flux, which changes the superconducting phase in the Josephson junction. In the MPMS SQUID VSM, magnetic fields up to 7T can be achieved using superconducting magnets.

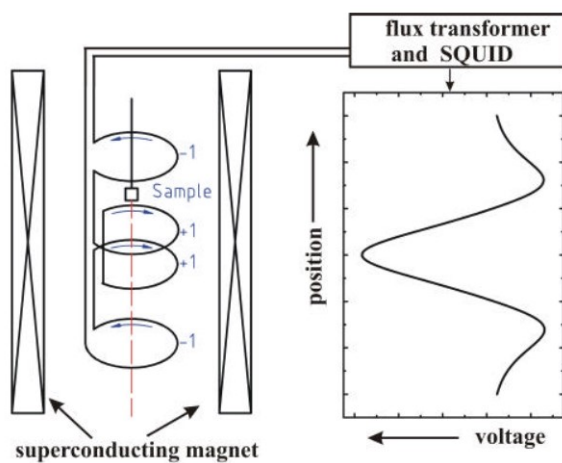


**Figure 2.6:** Pick-up-coil geometry and theoretical response signal of an ideal dipole vs scan length in an MPMS SQUID magnetometer. [6]

# Chapter 3

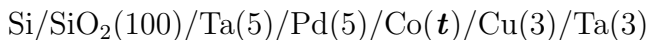
## Spin reorientation transition of Co in Pd/Co/Cu ultra-thin films.

### Objective

To determine the Spin-reorientation transition (SRT) thickness of Cobalt (Co).

### 3.1 Sample preparation

A series of thin film samples were prepared by varying the thickness of the FM layer ( $t_{Co}$ ) on Si/SiO<sub>2</sub>(001) substrate by DC magnetron sputtering in a high vacuum chamber with a base pressure better than  $1.6 \times 10^{-7}$  mbar. Due to the chamber's geometry, the angle between the substrate normal and the incident flux from the target is 30°. The sample structure is the following:



as shown in figure 3.1,

where the numbers in parentheses are the nominal thicknesses of corresponding layers in nanometers (figure 3.1).

During deposition, the thickness was monitored by a quartz crystal microbalance (QCM) mounted close to the substrate holder. The substrate was rotated at 10

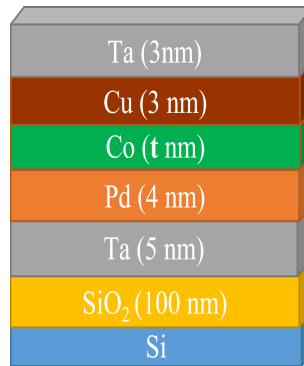


**Figure 3.1:** Schematic of sample structure.

rotations per minute (rpm) during deposition to get uniformity in the samples. A 5 nm thick Ta buffer layer was used for better adhesion and growth of the Pd layer along [111] direction. A 3 nm thick Ta was used as a capping layer to prevent oxidation. A series of 5 samples have been prepared with varying the Co thickness ranging from 0.62 nm to 1.25 nm as shown in table 3.1.

Table 3.1: Sample name and structure

Sample	Structure
S1	Si/SiO <sub>2</sub> /Ta(5)/Pd(4)/Co(0.62)/Cu(3)/Ta(3)
S2	Si/SiO <sub>2</sub> /Ta(5)/Pd(4)/Co(0.67)/Cu(3)/Ta(3)
S3	Si/SiO <sub>2</sub> /Ta(5)/Pd(4)/Co(0.72)/Cu(3)/Ta(3)
S4	Si/SiO <sub>2</sub> /Ta(5)/Pd(4)/Co(0.79)/Cu(3)/Ta(3)
S5	Si/SiO <sub>2</sub> /Ta(5)/Pd(4)/Co(0.89)/Cu(3)/Ta(3)

## 3.2 Structural characterization

To know the exact thickness and roughness of the deposited samples, we performed the XRR and the data was analysed using GenX software.

### 3.2.1 XRR analysis

XRR was performed for different samples, and each layer's respective thickness and roughness were found. In the figure, 3.2 samples with different cobalt thicknesses have been calibrated to the original thickness with the QCM thickness.

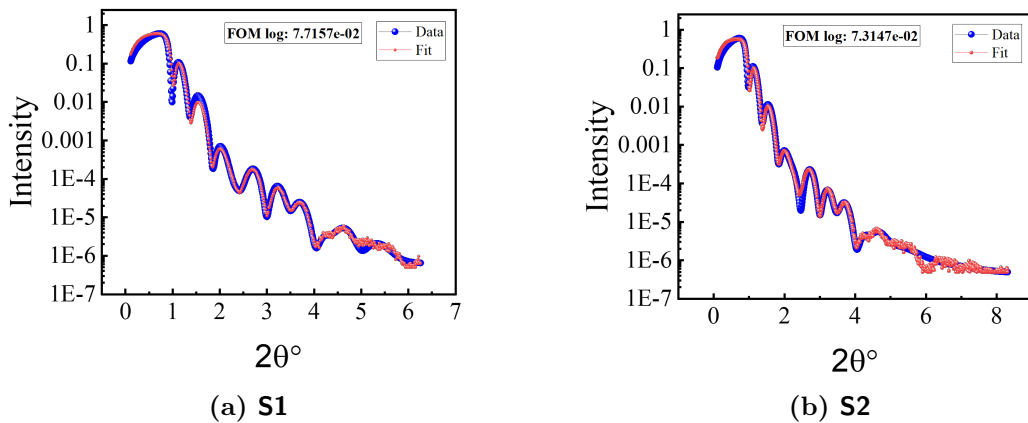


**Figure 3.2:** XRR fits of sample **S1** and **S2**.

During fitting the Keissig fringes we found that the Ta (capping layer) has formed its native oxide  $Ta_2O_5$ , and that resulted in some extra oscillations in the plot.

### 3.3 Study of magnetization reversal and effective anisotropy

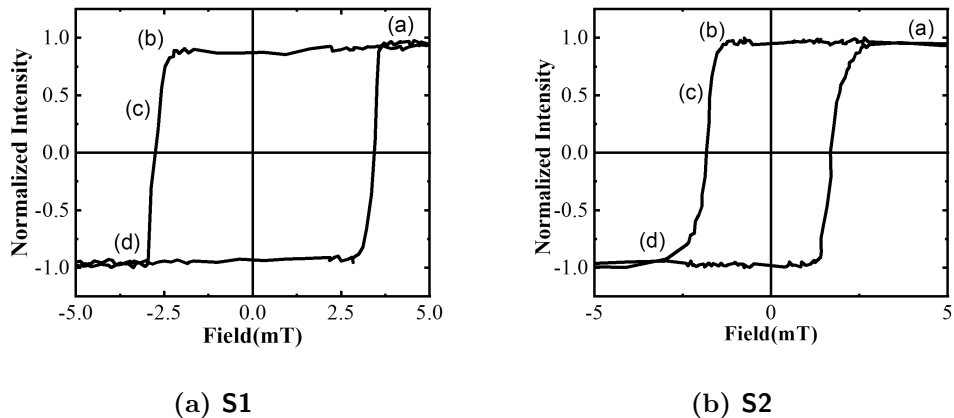
In this section we have used Kerr microscopy and SQUID to characterize the magnetic behavior of the samples.

All the samples were measured in both polar and longitudinal MOKE geometry.

### Polar MOKE measurement:

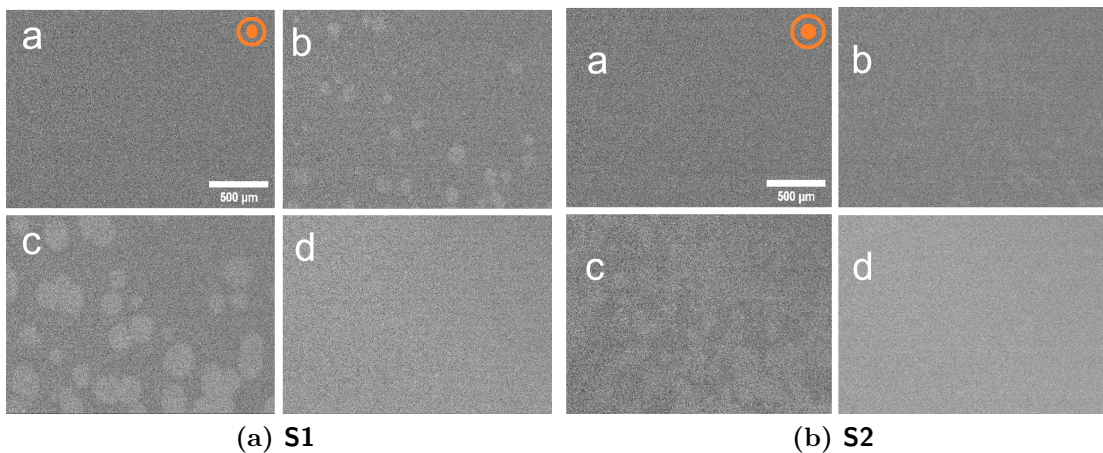
From figure 3.3, it can be seen that **S1** and **S2** form a hysteresis loop with saturation field ( $H_s$  less than 5 mT, on further increasing the thickness in **S3**, **S4** and **S5**, the hysteresis loop no longer saturate even at the highest field possible in the electromagnetic coil (figure3.3 (c),(d),(e)). The limitation of higher magnetic fields leads to changing the measurement technique. So for our experiment purpose, we shifted to the SQUID-VSM technique where the maximum field limit is 5 T.

For samples **S1** and **S2**, bubble domains were observed around the coercivity. (point (c) in **S1** and **S2**) as shown in figure 3.4, which marks the presence of perpendicular magnetic anisotropy (PMA) in the samples.



**Figure 3.3:** Polar MOKE measurement of the samples, where **S1** and **S2** have polar configuration as easy axis .

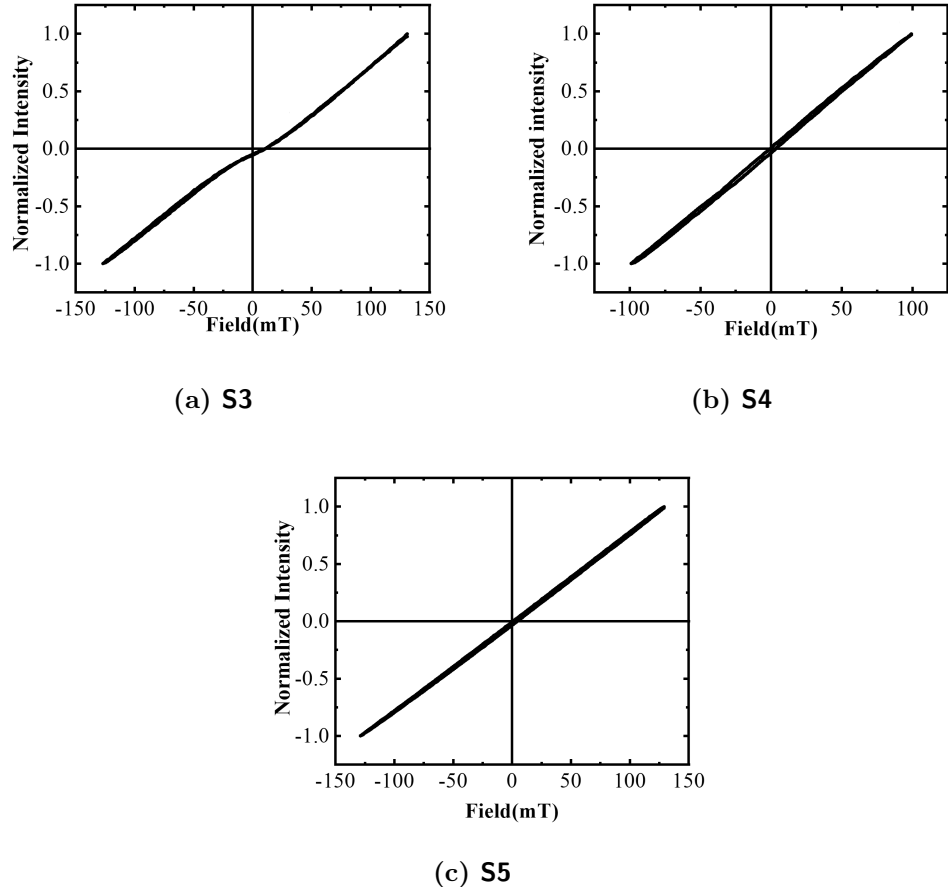
From figure 3.5, it could be inferred that samples **S3**, **S4**, and **S5** have hard axis normal to the sample surface (i.e. an in-plane easy axis). The hysteresis curves didn't have a saturation regime due to the limitations of the higher magnetic field in the Kerr-microscopy setup.



**Figure 3.4:** Kerr-microscopy images of **S1** and **S2** in polar MOKE geometry.  
Observed bubble domains around the coercivity (image (c))

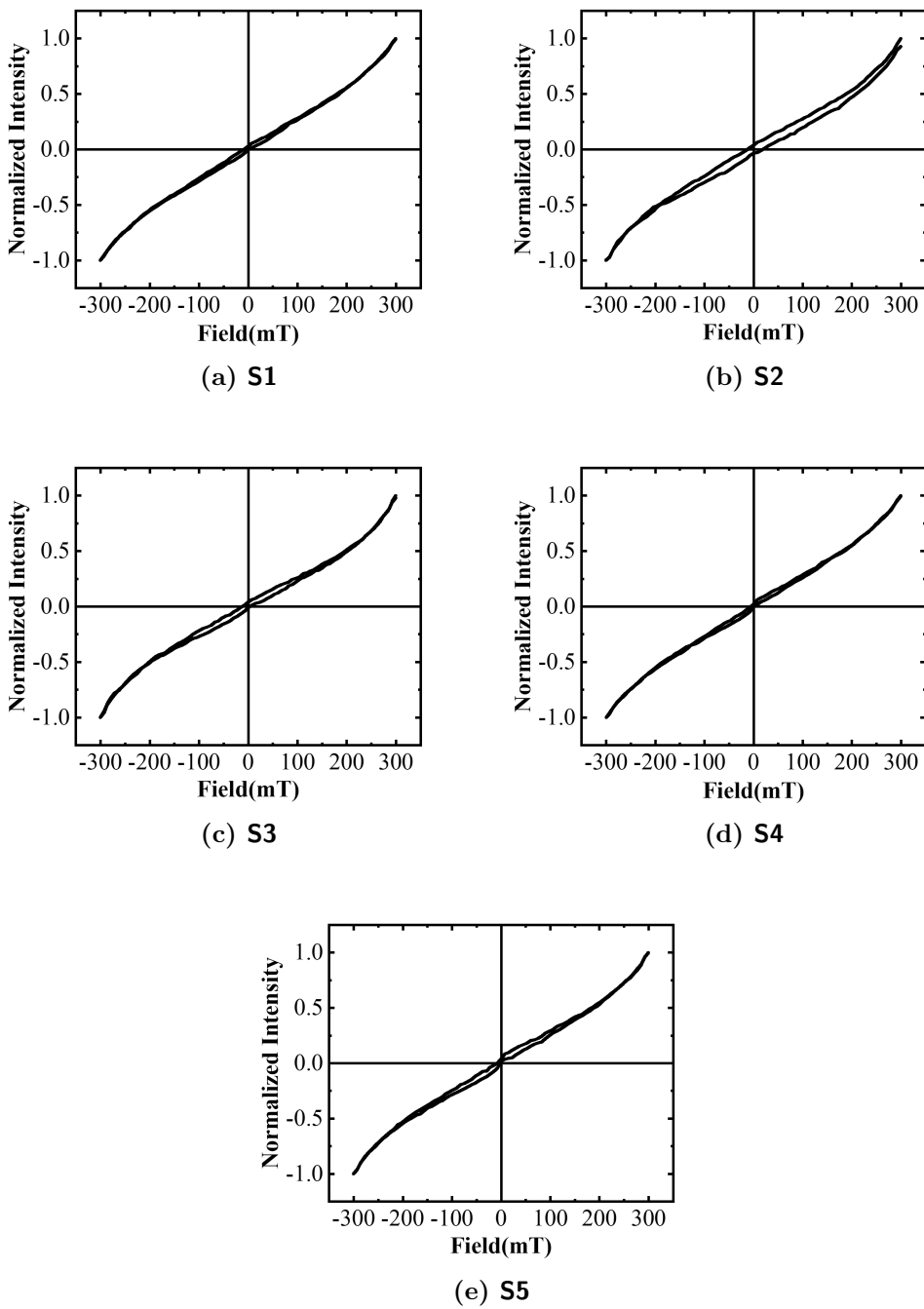
**Longitudinal MOKE measurement:**

Figure 3.6 shows that the samples didn't reach saturation magnetization, where the applied field is up to 300mT, which is the maximum field possible on the device.



**Figure 3.5:** Samples **S3**, **S4** and **S5** have hard axis as the polar configuration. The magnetization curve didn't saturate.

From figure 3.3 and figure 3.6, it was observed that due to the limitation of a higher magnetic field in the Kerr-microscope setup, the samples didn't reach the saturation magnetization for both the case of polar and longitudinal MOKE. Therefore we have performed both in-plane and out-of-plane measurements on SQUID and obtained the hysteresis loop.



**Figure 3.6:** Longitudinal MOKE measurement of the samples, the sample didn't saturate due to the instrumental constraint of a higher magnetic field.

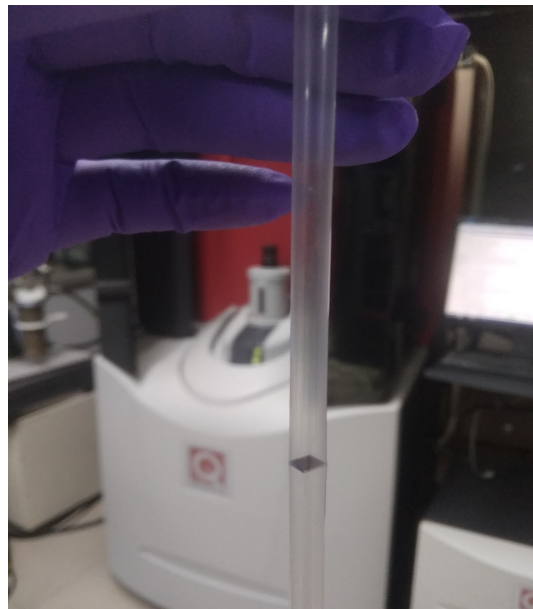


**Figure 3.7:** Sample mounted inside a straw for out-of-plane measurements.

#### **Out of plane measurement:**

In the out-of-plane configuration of SQUID, the magnetic field direction is normal to the sample. The sample is mounted inside a straw for measurement (figure 3.7). In SQUID, we performed the measurement at room temperature (300 K) and a maximum field of 1T, which was sufficient enough to reach the saturation magnetization regime.

From figure 3.8, it is observed that for the samples with PMA (**S1**, **S2**), the saturation field ( $H_s$ ) is less than 25 mT. For samples **S3**, **S4**, **S5** the saturation field ( $H_s$ ) is higher than 250 mT. From figure 3.8, we can infer that for samples **S1**, **S2**, the easy axis of magnetization lies perpendicular to the plane and lies in-plane for samples **S3**, **S4**, **S5**.

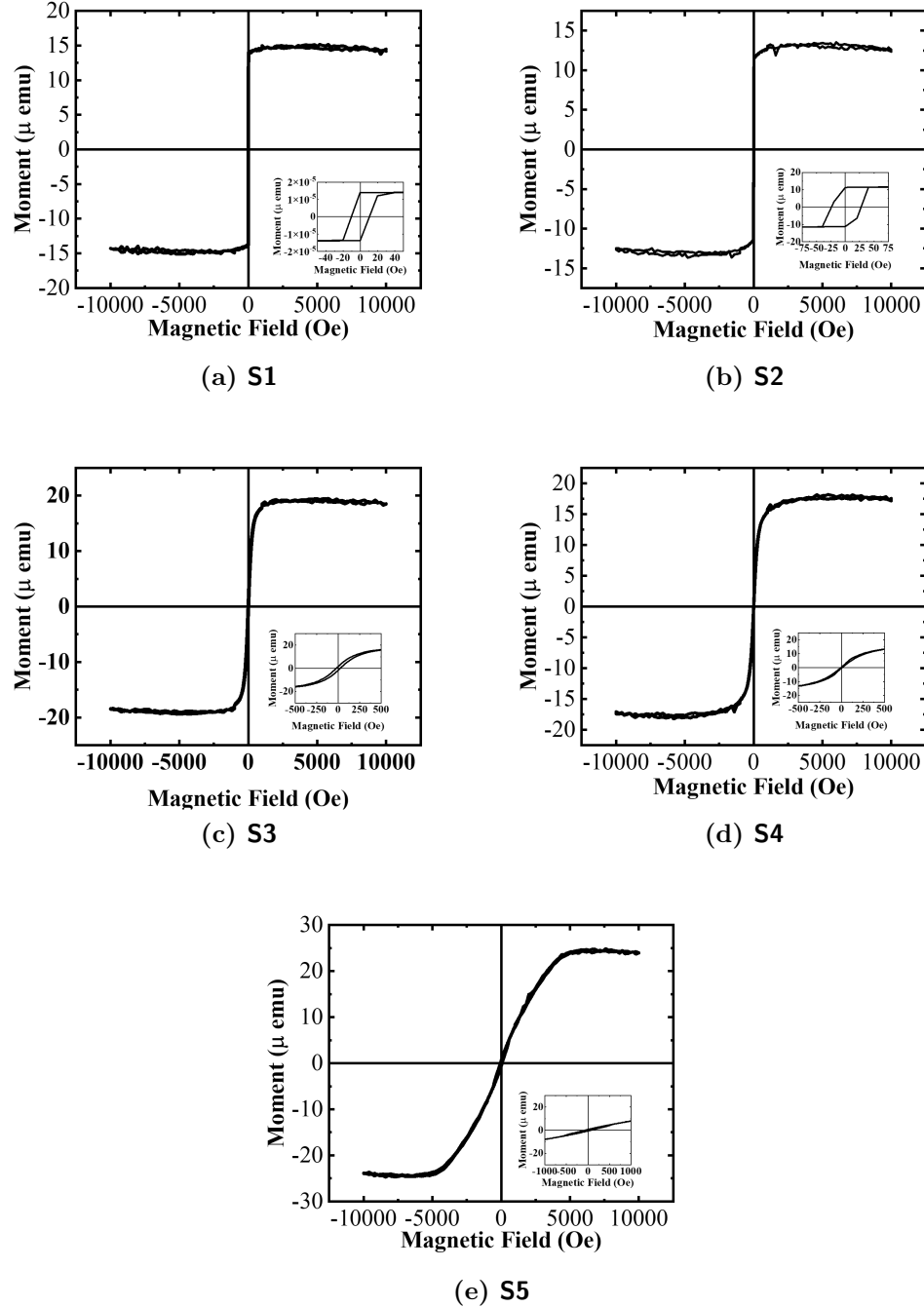


**Figure 3.8:** Magnetization reversal measured by SQUID-VSM (a) S1, (b) S2, (c) S3, (d) S4, (e) S5, where the magnetic field was applied perpendicular to the film at room temperature.



**Figure 3.9:** Sample mounted on quartz glass for in-plane measurement in SQUID magnetometry.

**In plane measurement:**

The in-plane measurements were performed in similar experimental conditions to out-of-plane measurements, at room temperature and magnetic field up to 1T. The samples were mounted on quartz glass for the in-plane magnetization reversal measurement in SQUID magnetometry.

From figure 3.10, we can infer that for samples **S1**, **S2**, the magnetization easy axis lies normal to the sample surface and for samples **S3**, **S4**, **S5** it lies in-plane.

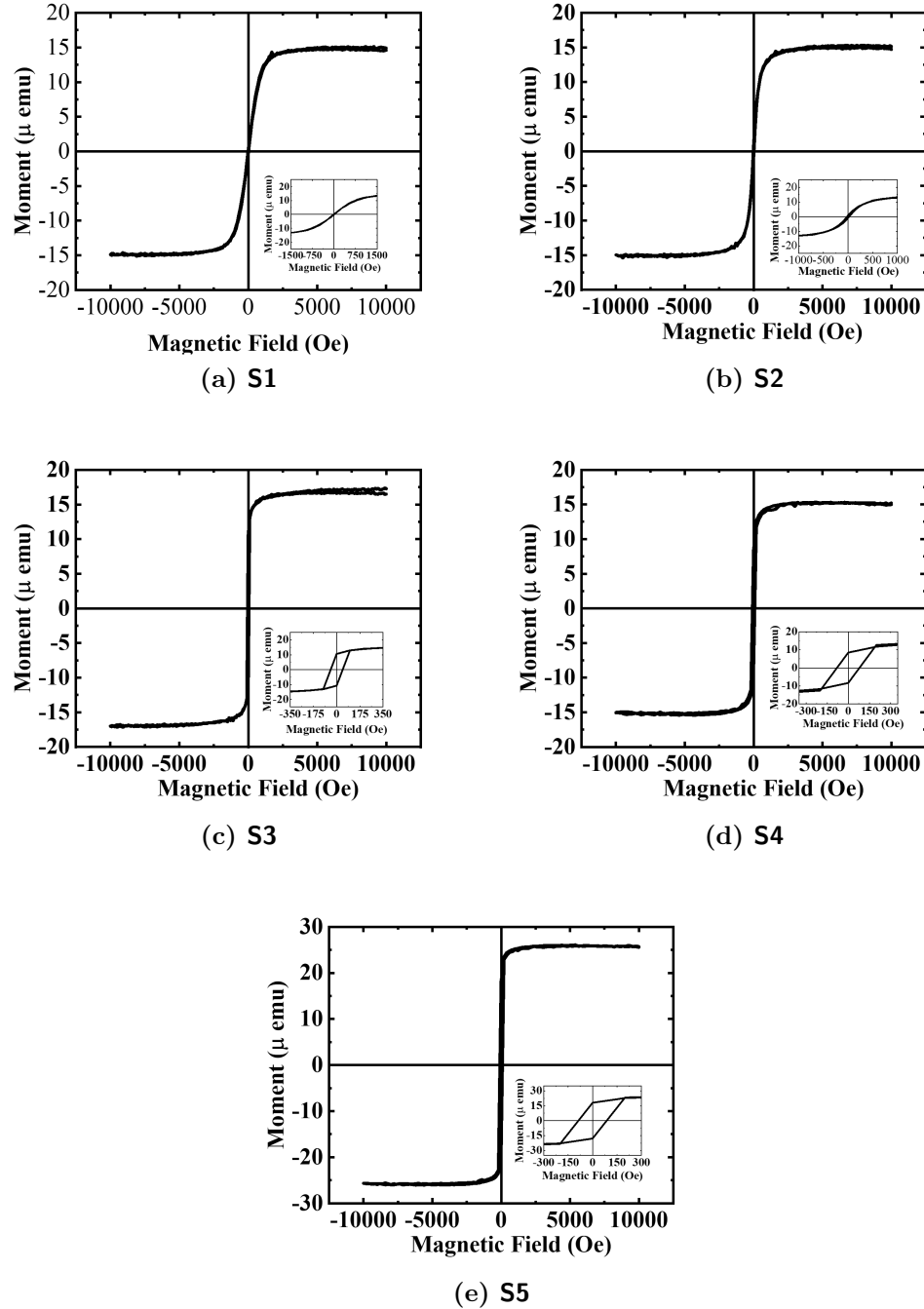


**Figure 3.10:** Magnetization reversal measured by SQUID-VSM (a) **S1**, (b) **S2**, (c) **S3**, (d) **S4**, (e) **S5**, where the magnetic field was applied in-plane to the film at room temperature.

The effective anisotropy in our samples has been calculated using the following formula:

$$K_{eff} = \frac{1}{2}\mu_o H_{eff} M_s \quad (3.1)$$

where  $\mu_o$  is the permeability of free space.

$H_{eff}$  is the hard axis saturation field minus easy axis saturation field.

$M_s$  is the saturation magnetization.

figure 3.11 shows the calculation of  $K_{eff}$ .

For samples **S1**, **S2**, **S3**, **S4** and **S5** the respective saturation magnetization values are:

$$M_S(\mathbf{S1}) = 1.48 \times 10^6 A/m$$

$$M_S(\mathbf{S2}) = 1.25 \times 10^6 A/m$$

$$M_S(\mathbf{S3}) = 1.45 \times 10^6 A/m$$

$$M_S(\mathbf{S4}) = 1.36 \times 10^6 A/m$$

$$M_S(\mathbf{S5}) = 1.59 \times 10^6 A/m$$

The effective anisotropy for the samples **S1**, **S2**, **S3**, **S4** and **S5** were calculated to be as:

$$K_{eff}(\mathbf{S1}) = 7.09 \times 10^5 J/m^3$$

$$K_{eff}(\mathbf{S2}) = 5.51 \times 10^5 J/m^3$$

$$K_{eff}(\mathbf{S3}) = -3.19 \times 10^5 J/m^3$$

$$K_{eff}(\mathbf{S4}) = -6.26 \times 10^5 J/m^3$$

$$K_{eff}(\mathbf{S5}) = 7.09 \times 10^5 J/m^3$$

$t'_\text{Co}$ (nm)	$M_s$ (A/m)	$\mu_0 H_s$ (T)	$K_{eff} = \frac{1}{2} \mu_0 H_s$ (J/m <sup>3</sup> )
0.62	$1.48 \times 10^6$	0.48	$7.09 \times 10^5$
0.67	$1.25 \times 10^6$	0.36	$5.51 \times 10^5$
0.72	$1.45 \times 10^6$	-0.22	$-3.19 \times 10^5$
0.79	$1.36 \times 10^6$	-0.46	$-6.26 \times 10^5$
0.89	$1.59 \times 10^6$	-0.60	$-9.54 \times 10^5$

**Figure 3.11:** Calculation of effective anisotropy ( $K_{eff}$ ).

On plotting  $t.K_{eff}$  vs  $t$  (figure 3.12) and fitting it linearly shows the transition ( $K_{eff} = 0$ ) from in-plane to the out-of-plane occurs at  $\tilde{0.7}$  nm (i.e. the SRT thickness). From the slope of the line in figure 3.12 we estimate that  $K_\nu = -5.13 \times 10^6 J/m^3$ .

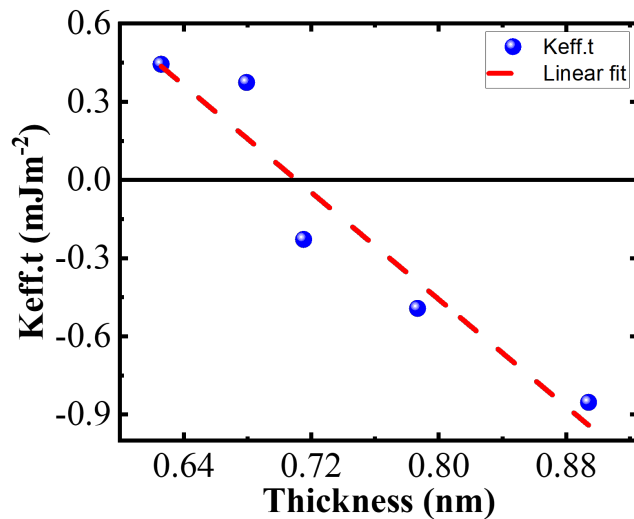


**Figure 3.12:**  $t.K_{eff}$  vs  $t$  plot, SRT for Cobalt is observed around 0.70 nm.

The SRT thickness of Cobalt is similar to the value reported by Garcia et al. [33]. They found that in Pd/Co multilayered system, the transition of magnetization from PMA to in-plane occurs when  $t_{Co} < 8\text{\AA}$  (figure 3.13). Further, the authors have

claimed that surface anisotropy at Pd/Co interfaces and strain in Co layers cause the perpendicular easy axis rather than crystalline anisotropy and on the other hand, the positive value of  $K_u$  (total anisotropy energy) indicates the existence of PMA in the sample whereas positive values of  $K_s$  (surface anisotropy energy) and  $K_v$  (volume anisotropy energy) favour in-plane magnetization.

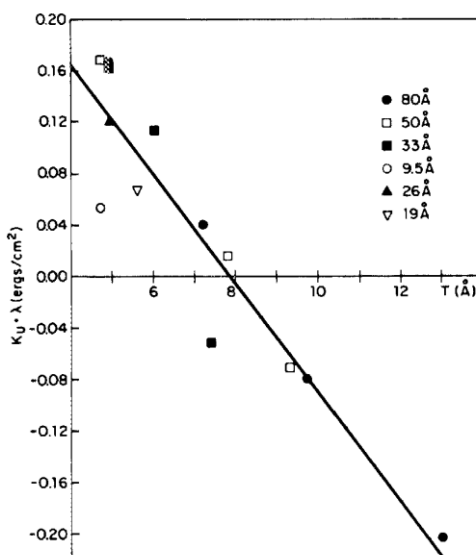


**Figure 3.13:** Total anisotropy energy  $K_u$  multiplied by the bilayer period  $\lambda$  vs the Co layer thickness  $t$ . Symbols denote experimental data for different Pd thicknesses. The solid line is linear fit

# Chapter 4

## Voltage-controlled magnetic anisotropy in perpendicularly magnetized Pt/Co/Pt ultrathin films

### Objective

To achieve voltage-induced modulation magnetic properties (anisotropy, domain behaviour, interfacial exchange interaction) in Pt/Co/Pt thin-Films.

#### 4.1 Sample preparation

A series of samples have been prepared by varying the ferromagnetic (FM) layer thickness ( $t_{Co}$ ); the complete sample structure is as follows:

##### Sample 1:

Si (sub)/ Ta (3 nm)/ Pt (3.5 nm)/ Co (0.8 nm)/ Pt (0.5 nm)/ MgO (14 nm)/ Pt (5 nm)

##### Sample 2:

Si (sub)/ Ta (3 nm)/ Pt (5 nm)/ Ta (3 nm)/ Pt (3.5 nm)/ Co (1.3 nm)/ Pt (0.5 nm)/ MgO (14 nm)/ Pt (5 nm)

The samples are labelled as: **S<sub>1</sub>** & **S<sub>2</sub>**

Before mounting the substrate for deposition, all the sides of the substrate were covered with Kapton and double-sided tape to avoid deposition along the edges, thus avoiding the chances of short-circuiting between the top and bottom layer, as shown in Figure 4.1

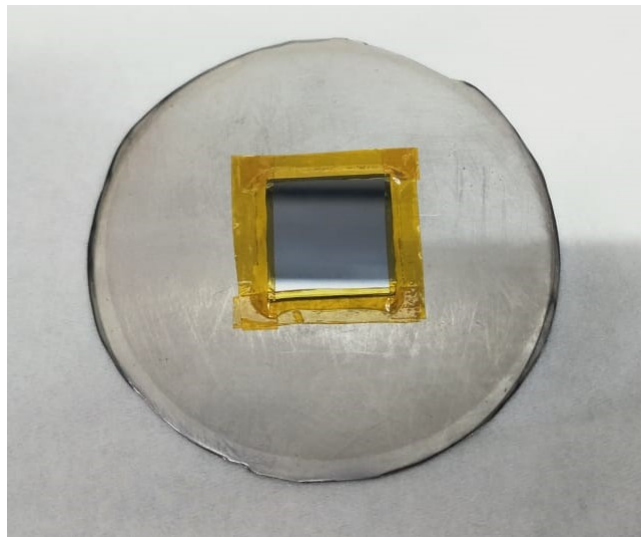


**Figure 4.1:** Edge-covered substrate before deposition.

The samples are deposited on an n-type Si substrate with resistance in the order of  $\sim 10^6 \Omega$ . All the metallic layers(Ta, Pt, Co) are deposited by DC magnetron sputtering, and the metal oxide (MgO) layer is deposited by RF sputtering. The base pressure before the deposition was better than  $7.4 \times 10^{-8}$  mbar and the deposition pressure was  $1.6 \times 10^{-3}$  mbar in a high-vacuum multi-deposition chamber. The substrate table was rotated at 15 rotations per minute (rpm) during deposition to get uniformity in the sample. During the deposition thickness of the layers was monitored by a Quartz crystal microbalance (QCM) mounted close to the substrate holder.

Here Ta acts as a seed layer for the growth of Pt along [111] direction. Ta/Pt layer

has been deposited on the back side of the Si substrate for proper charge distribution on the bottom surface (of Silicon substrate) as well as to make wire contacts between the top and bottom (Pt (20 nm)) layers to perform VCMA measurements Figure 4.2(a).

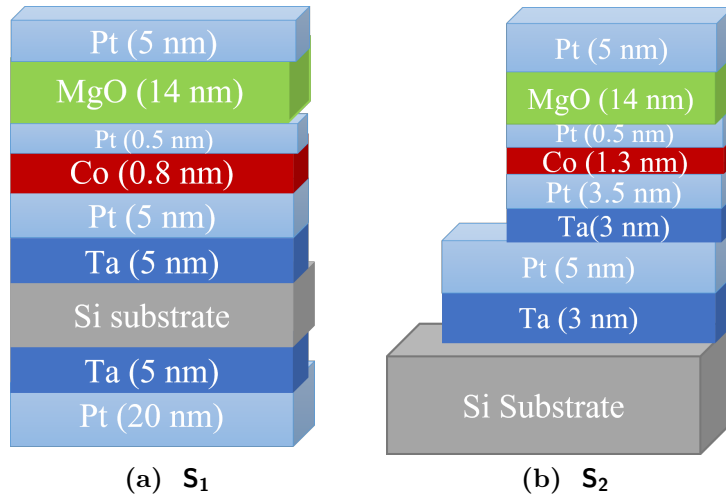


**Figure 4.2:** Schematic of sample structure

## 4.2 VCMA measurement

To investigate the voltage-controlled magnetic anisotropy (VCMA) effect, capacitive contact was established using a Magneto-resistance holder, as illustrated in Figure 4.3. The first point of contact was established on the uppermost surface of the sample using silver paste. A multi-step process was employed for the second point of contact, located on the bottom surface.

First, the holder region was insulated using electrical tape, after which copper tape was affixed to the insulating surface to establish conductive contact with the sample. Finally, the Silver paste was used to establish the ultimate contact between the sample's bottom surface and the copper tape. In addition, we used a soldering iron to

establish contact at gate numbers 3 and 8, to apply voltage (4.3). After making all the contacts, the continuity of the setup is cross-checked using a multimeter.

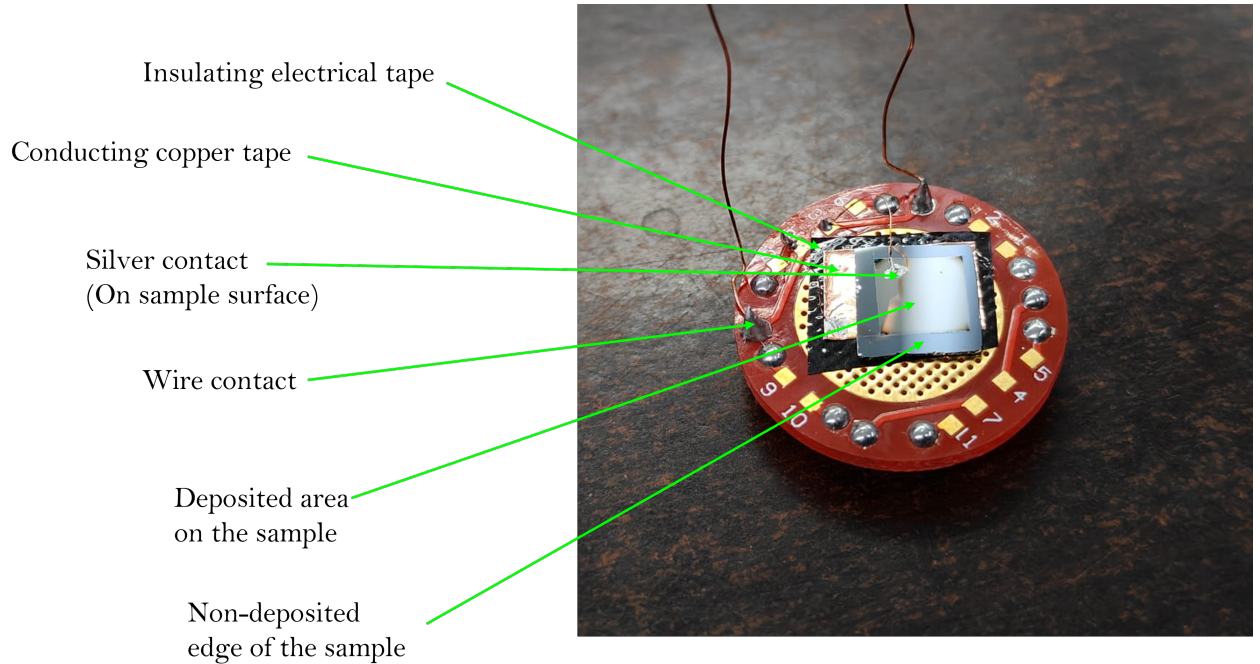


**Figure 4.3:** The VCMA setup

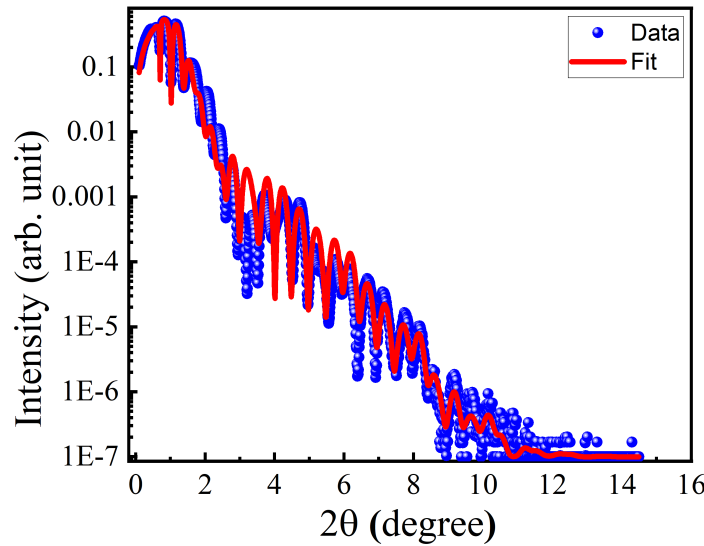
To study the magnetization reversal and domain wall dynamics under the application of voltage, Magneto-optic Kerr effect-based microscopy is performed in the polar configuration. The voltage is applied using a source meter.

## 4.3 Structural characterization

### 4.3.1 XRR analysis

X-ray reflectivity (XRR) measurements have been performed using an X-ray diffractometer to quantify the multilayered sample's structural parameters, such as thickness, density and roughness. Figure 4.4 shows the XRR fit of the sample **S<sub>1</sub>** and the

fitted parameters are shown in table 4.1.



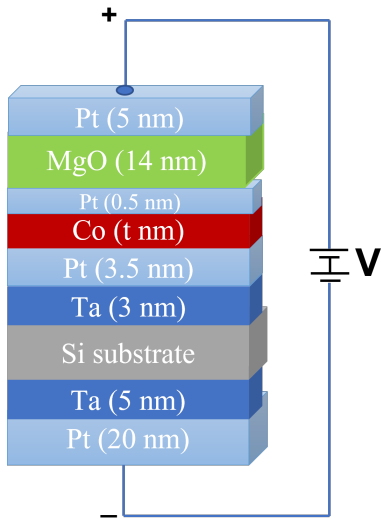
**Figure 4.4:** XRR fit of sample  $S_1$

Table 4.1:  $S_1$  XRR fit parameters.

Layer	Thickness (nm)	Roughness (nm)
Ta	2	0.31
Pt	3.74	0.47
Co	0.68	0.32
Pt	0.62	0.42
MgO	13.5	0.99
Pt	3.75	0.43

## 4.4 Magnetic characterization

For sample,  $S_1$  magnetic characterization has been performed by applying a voltage across the top and bottom layer as shown in Figure 4.5.



**Figure 4.5:** Schematic of **S<sub>1</sub>** with applied bias voltage.

#### 4.4.1 Magnetization reversal with voltage application

##### In sample S<sub>1</sub>

In this section, the Kerr microscopy technique is used to characterize the magnetic behaviour of the samples with and without applying voltages of varied amplitude.

Hysteresis loops measured using MOKE microscopy in polar configuration shows square shaped loop, which confirms the (Figure 4.6), the existence of PMA in the sample as it was expected as the thickness of Co is far away from spin-reorientation transition (SRT) [34].

The magnetic coercivity diminishes with an upsurge in negative polarity voltage, as revealed by the plot in Figure 4.7, indicating the presence of the VCMA effect. Notably, no alteration in the loop is observed at 0V and -20V; however, at -50V, a reduction in coercivity is noticeable, and this trend persists up to -100 V (which corresponds to the maximum limit of the source meter). Exposing the sample to a high voltage could result in a breakdown and trigger an upsurge in current, ultimately

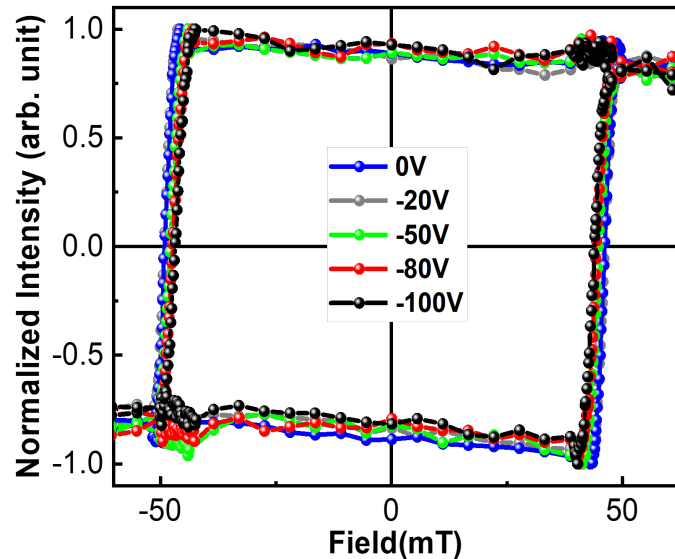


**Figure 4.6:** Magnetic hysteresis loop measure by polar MOKE microscopy of  $S_1$  with varying voltage.

causing permanent damage to the sample due to overheating. Table 4.2 represents the coercive field values associated with the applied bias voltages. The highest variation in coercivity amounts to 2.33 mT between 0 V and -100 V.

Table 4.2: Coercive field values at the respective voltage for sample  $S_1$

Sl.no	Voltage (V)	Coercive field (mT)
1	0	46.18
2	-20	46.19
3	-50	44.83
4	-80	44.41
5	-100	43.85

In R.A. One et al., the cause of the shift in coercivity is described, along with two

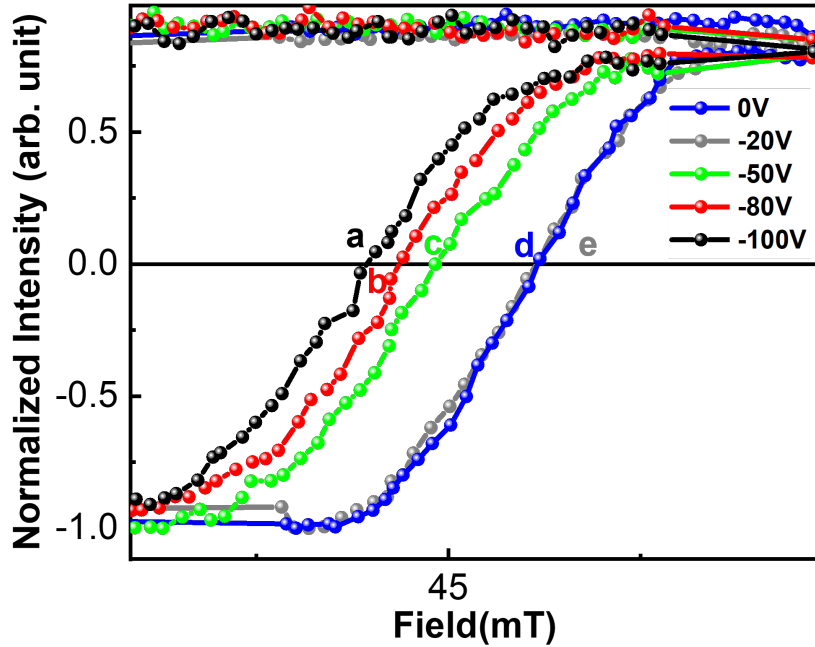


**Figure 4.7:** Zoomed Fig 4.6 to observe the change in coercivity with voltage.

contributing factors. First, the applied E-field has a surface charge doping effect that alters the relative occupation of the electronic orbitals at the interface. The effect is mainly localized at the interface due to the limited penetration of the field in the metal. Second, the E-field influences the interfacial intrinsic dipole field. Therefore, the anisotropy energy is not located at the interface but propagates in bulk like a damped wave. These two main mechanisms lead to an asymmetric effect of the E-field on the PMA with respect to the E-field polarity: an increase in the PMA for a given polarity and a decrease in the PMA when the polarity is reversed [35].

To observe the change in magnetic domains with the VCMA effect, domain images were extracted at the coercivity of the hysteresis loop at respective voltages, as shown

in Figure 4.8. It can be seen that there is a very nominal change in the shape of the domains w.r.t the applied voltage (marked by the "red rings"). It is understood that for 0.8 nm Cobalt, such a change in coercivity doesn't affect the magnetic domains significantly.

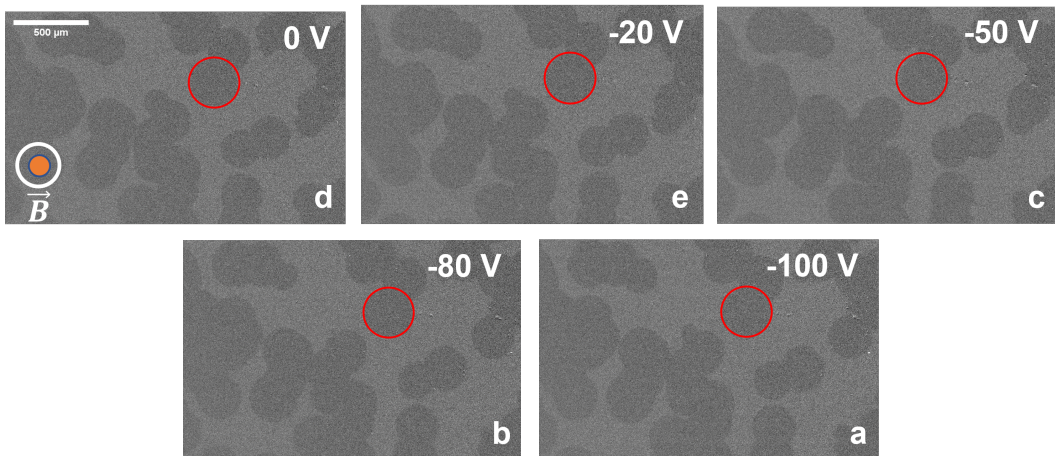


**Figure 4.8:**  $\mathbf{S}_1$  magnetic domain images at the coercivity at respective voltages.

The sample  $\mathbf{S}_2$  was prepared with slight modifications to overcome the challenges that were faced during  $\mathbf{S}_1$  measurement. First, the application of bias voltage in positive polarity was difficult due to the diode-like behaviour of the Silicon (Si) substrate, which caused it to act in forward bias mode, thus leading to high current flow ( $\sim 1A$ ). Second, higher voltages had to be applied to observe the VCMA effect, as the thickness of the substrate could have been one of the reasons for the decrement in the effective electric field. Therefore for  $\mathbf{S}_2$ , measurements were done in two modes, as shown in Figure 4.9. For the first measurement, contact between the top of Si substrate and the sample surface is made in Figure 4.9 (a).

For the second measurement, an extra layer of Ta/Pt is grown, and after masking a small area with Kapton tape, then the original structure ( $\mathbf{S}_1$ ) is deposited as shown in Figure 4.9 (b) keeping  $t_{Co} = 1.3nm$ . The contact between the sample surface and

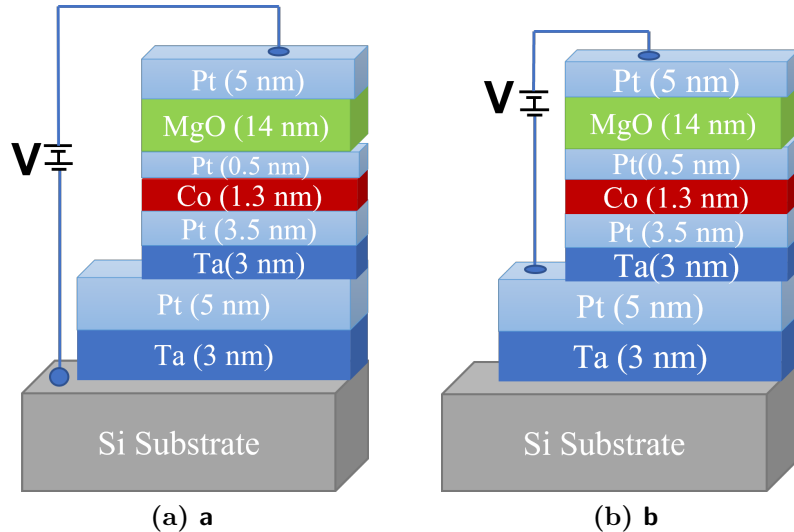


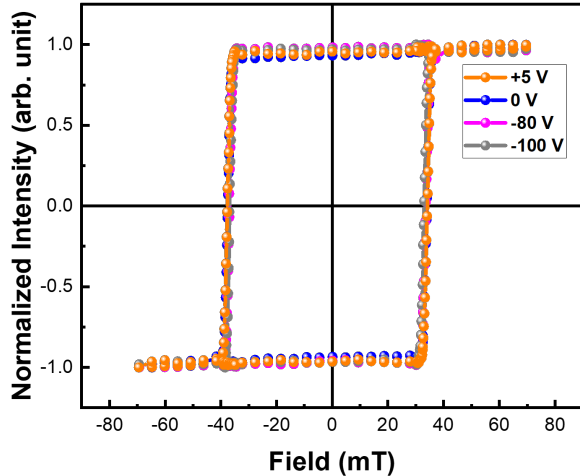
**Figure 4.9:** Schematic of **S<sub>2</sub>** with applied bias voltage.

the Pt/Ta layer is made.

### In sample **S<sub>2</sub>**

The polar MOKE hysteresis loop for sample **S<sub>2</sub>** under the application of voltage is shown in Figure 4.10. From the hysteresis loop, it can be inferred that the sample does not reach SRT even after increasing Co thickness due to the [Ta/Pt]<sub>2</sub> stack deposition.

The change in the coercivity of **S<sub>2</sub>** with voltage can be observed more prominently in Figure 4.11. Similar to the previous case (for **S<sub>1</sub>**), here also, the VCMA effect arises with higher negative voltage. However, an increase in coercivity has been observed by applying a positive voltage which wasn't seen in the previous case. Thus tuning the magnetization reversal process in both directions was possible by applying opposite voltages, which is also reversible. Table 7.3 represents the coercive field values associated with the applied bias voltages. The highest variation in coercivity amounts to 1.21 mT between 5 V and -100 V.



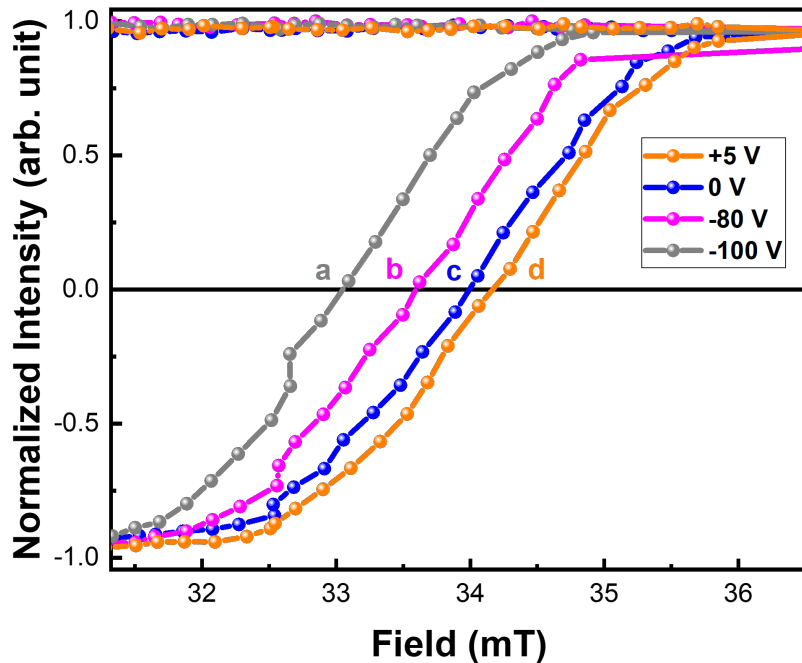
**Figure 4.10:** Magnetic hysteresis loop measured by polar MOKE microscopy of **S<sub>2</sub>** with varying voltage.

Table 4.3: Coercive field values at the respective voltage for sample S<sub>2</sub>

Sl.no	Voltage (V)	Coercive field (mT)
1	+5	34.30
2	0	34.05
3	-80	33.62
4	-100	33.09

The change in magnetic domain behaviour with the VCMA effect was analyzed. The marked "yellow ring" in Figure 4.12 indicates the change in magnetic domain size from positive to negative bias. As the voltage in negative polarity keeps increasing, the domain's size also increases. This change was not observed in the case of sample S<sub>1</sub>.

However, earlier limitations still arose during the experiment as comparatively application of the same voltage in positive polarity wasn't possible (i.e. still high current flow was observed). The second measurement configuration 4.9(b) was used to ensure that the problem arising was due to the substrate or not.



**Figure 4.11:** Zoomed Fig 4.10 to observe the change in coercivity with voltage.

#### Measurement in Ta/Pt contact

When the measurement was performed between Ta/Pt and the sample surface, a comparatively high current flow was found at the same applied voltage. However, on applying lower voltages, the change in the hysteresis loop was less significant and cannot be marked by a shift in magnetization reversal with opposite polarity voltages. This clarified our doubts about the substrate causing problem. Investigating further, in a very recent paper by OP Das et al. there, it has been mentioned that as voltage increases from 0V, the sample continues to be in a high resistive state (HRS), but as the voltage increases and reaches a particular value  $V_{SET}$  oxygen atoms start to detach from the metal atom (Mg), and oxygen vacancies evolve. Due to the positive applied voltage, the negatively charged oxygen ions migrate from the oxide ( $MgO$ ) to-

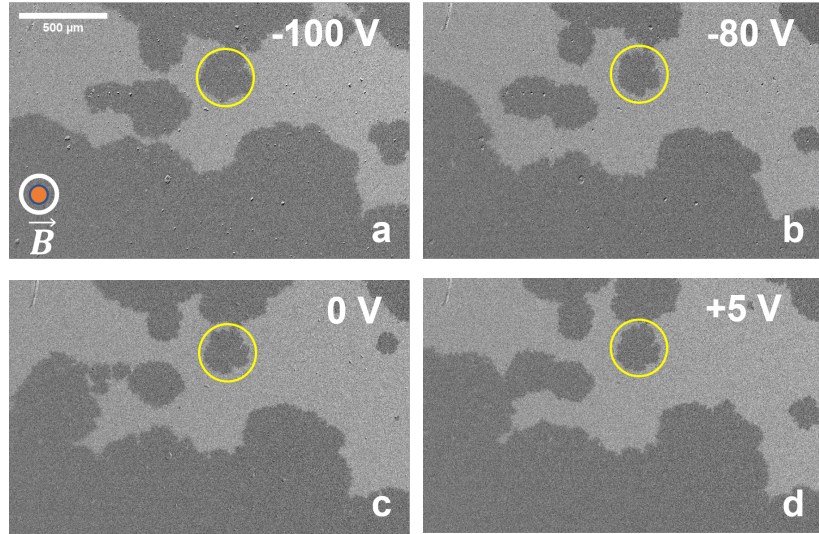


**Figure 4.12:**  $\mathbf{S}_2$  magnetic domain images at the coercivity at respective voltages.

wards the top electrode interface. This oxygen migration creates vacancies inside the oxide, arranged to form a nano-filament under the influence of a high electric field. [36]

Therefore measurements on this configuration (4.9(b)) have been avoided, as passing high current will lead to heating of the sample, thereby permanently damaging the sample.

# Chapter 5

## Summary and Conclusions

In conclusion, we have systematically studied and determined the SRT of Cobalt in Pd/Co/Cu ultrathin films by varying the thickness of Co from 0.62 nm to 1.25 nm and the VCMA effect in Pt/Co/Pt ultrathin films by varying the Co thickness and the applied voltage. For the first part, we observed that spontaneous magnetization switches from out-of-plane (PMA) to in-plane direction with increasing thickness. The nominal SRT thickness for Co in Pd/Co/Cu system is found to be 0.70 nm (figure 3.12).

For the second part, samples near and far from SRT were made by varying  $t_{Co}$ ; their magnetic hysteresis loops and respective domain images at the coercivity were recorded by the Kerr-microscopy technique at different voltages. A reduction in the effective PMA of the samples corroborates the observation of a decrement in coercivity with increasing negative polarity voltage. The maximum change in the coercivity is found as 2.33 mT and 1.21 mT for samples **S<sub>1</sub>** and **S<sub>2</sub>**; coercivity change got reduced in **S<sub>2</sub>** as the addition of [Ta/Pt]<sub>2</sub> stack enhanced the PMA. In **S<sub>2</sub>**, we observed that the size of domains increases with the increase in voltage. The surface charge doping effect and the influence of the interfacial intrinsic dipole field seem to play the key role in the VCMA effect [35].

Comparative high current flow for positive bias voltage caused a limitation to our experiment; however, its possible origin could be due to the filament formation in

---

*5 Summary and Conclusions*

the MgO layer as discussed by OP Das et al. [36]. Some of the factors that can be adjusted to achieve an enhancement in VCMA, such as the unavailability of charges across the sample, could be modified with ionic gels or ionic liquids to generate a proper electric field [9], adjustment of the sample thickness to a level close to SRT, allowing for magnetization switching. Novel approaches to modifying these factors will pave the way for developing application-oriented devices.

# References

- [1] T. Nozaki, T. Yamamoto, S. Miwa, M. Tsujikawa, M. Shirai, S. Yuasa, and Y. Suzuki, “Recent progress in the voltage-controlled magnetic anisotropy effect and the challenges faced in developing voltage-torque mram,” *Micromachines*, vol. 10, no. 5, p. 327, 2019.
- [2] N. A. Spaldin, *Magnetic Materials: Fundamentals and Applications*. Cambridge University Press, 2 ed., 2010.
- [3] D. Wilgocka-Ślezak, K. Freindl, A. Kozioł, K. Matlak, M. Rams, N. Spiridis, M. Ślezak, T. Ślezak, M. Zajac, and J. Korecki, “Thickness-driven polar spin reorientation transition in ultrathin fe/au (001) films,” *Physical Review B*, vol. 81, no. 6, p. 064421, 2010.
- [4] B. Miao, Y. Millev, L. Sun, B. You, W. Zhang, and H. Ding, “Thickness-driven spin reorientation transition in ultrathin films,” *Science China Physics, Mechanics and Astronomy*, vol. 56, no. 1, pp. 70–84, 2013.
- [5] M. Yasaka *et al.*, “X-ray thin-film measurement techniques,” *The Rigaku Journal*, vol. 26, no. 2, pp. 1–9, 2010.
- [6] S. Bedanta, *Supermagnetism in magnetic nanoparticle systems (Supermagnetismus in magnetischen Nanoteilchensystemen)*. PhD thesis, PhD thesis, 2006.
- [7] R. Tomasello, E. Martinez, R. Zivieri, L. Torres, M. Carpentieri, and G. Finocchio, “A strategy for the design of skyrmion racetrack memories,” *Scientific reports*, vol. 4, no. 1, pp. 1–7, 2014.

- [8] A. Fert, N. Reyren, and V. Cros, “Magnetic skyrmions: advances in physics and potential applications,” *Nature Reviews Materials*, vol. 2, no. 7, pp. 1–15, 2017.
- [9] M. Weisheit, S. Fähler, A. Marty, Y. Souche, C. Poinsignon, and D. Givord, “Electric field-induced modification of magnetism in thin-film ferromagnets,” *Science*, vol. 315, no. 5810, pp. 349–351, 2007.
- [10] T. Maruyama, Y. Shiota, T. Nozaki, K. Ohta, N. Toda, M. Mizuguchi, A. Tulapurkar, T. Shinjo, M. Shiraishi, S. Mizukami, *et al.*, “Large voltage-induced magnetic anisotropy change in a few atomic layers of iron,” *Nature nanotechnology*, vol. 4, no. 3, pp. 158–161, 2009.
- [11] T. Kawabe, K. Yoshikawa, M. Tsujikawa, T. Tsukahara, K. Nawaoka, Y. Kotani, K. Toyoki, M. Goto, M. Suzuki, T. Nakamura, *et al.*, “Electric-field-induced changes of magnetic moments and magnetocrystalline anisotropy in ultrathin cobalt films,” *Physical Review B*, vol. 96, no. 22, p. 220412, 2017.
- [12] B. Dieny and M. Chshiev, “Perpendicular magnetic anisotropy at transition metal/oxide interfaces and applications,” *Reviews of Modern Physics*, vol. 89, no. 2, p. 025008, 2017.
- [13] A. Hubert and R. Schäfer, *Magnetic domains: the analysis of magnetic microstructures*. Springer Science & Business Media, 2008.
- [14] M. Akyol, “Origin of interfacial magnetic anisotropy in ta/cofeb/mgo and pt/cofeb/mgo multilayer thin film stacks,” *Journal of Superconductivity and Novel Magnetism*, vol. 32, pp. 457–462, 2019.
- [15] S. Ikeda, K. Miura, H. Yamamoto, K. Mizunuma, H. Gan, M. Endo, S. Kanai, J. Hayakawa, F. Matsukura, and H. Ohno, “A perpendicular-anisotropy cofeb–

- mgo magnetic tunnel junction,” *Nature materials*, vol. 9, no. 9, pp. 721–724, 2010.
- [16] A. Manchon, S. Pizzini, J. Vogel, V. Uhlir, L. Lombard, C. Ducruet, S. Auffret, B. Rodmacq, B. Dieny, M. Hochstrasser, *et al.*, “X-ray analysis of the magnetic influence of oxygen in pt/ co/ al o x trilayers,” *Journal of Applied Physics*, vol. 103, no. 7, p. 07A912, 2008.
- [17] D. Chiba, S. Fukami, K. Shimamura, N. Ishiwata, K. Kobayashi, and T. Ono, “Electrical control of the ferromagnetic phase transition in cobalt at room temperature,” *Nature materials*, vol. 10, no. 11, pp. 853–856, 2011.
- [18] M. Oba, K. Nakamura, T. Akiyama, T. Ito, M. Weinert, and A. Freeman, “Electric-field-induced modification of the magnon energy, exchange interaction, and curie temperature of transition-metal thin films,” *Physical review letters*, vol. 114, no. 10, p. 107202, 2015.
- [19] P. Borisov, A. Hochstrat, X. Chen, W. Kleemann, and C. Binek, “Magnetolectric switching of exchange bias,” *Physical review letters*, vol. 94, no. 11, p. 117203, 2005.
- [20] X.-Z. Lu and J. M. Rondinelli, “Tunable magnetic anisotropy in multiferroic oxides,” *Physical Review B*, vol. 103, no. 18, p. 184417, 2021.
- [21] H. Nakayama, T. Nozaki, T. Nozaki, and S. Yuasa, “Engineering co/mgo interface with heavy metals for voltage-controlled magnetic anisotropy effect,” *Applied Physics Letters*, vol. 122, no. 3, p. 032403, 2023.

- [22] M. Endo, S. Kanai, S. Ikeda, F. Matsukura, and H. Ohno, “Electric-field effects on thickness dependent magnetic anisotropy of sputtered mgo/co 40 fe 40 b 20/ta structures,” *Applied Physics Letters*, vol. 96, no. 21, p. 212503, 2010.
- [23] T. Nozaki, Y. Shiota, M. Shiraishi, T. Shinjo, and Y. Suzuki, “Voltage-induced perpendicular magnetic anisotropy change in magnetic tunnel junctions,” *Applied Physics Letters*, vol. 96, no. 2, p. 022506, 2010.
- [24] S. Kanai, M. Yamanouchi, S. Ikeda, Y. Nakatani, F. Matsukura, and H. Ohno, “Electric field-induced magnetization reversal in a perpendicular-anisotropy cofeb-mgo magnetic tunnel junction,” *Applied Physics Letters*, vol. 101, no. 12, p. 122403, 2012.
- [25] F. Bonell, Y. Takahashi, D. Lam, S. Yoshida, Y. Shiota, S. Miwa, T. Nakamura, and Y. Suzuki, “Reversible change in the oxidation state and magnetic circular dichroism of fe driven by an electric field at the feco/mgo interface,” *Applied Physics Letters*, vol. 102, no. 15, p. 152401, 2013.
- [26] G. Yu, Z. Wang, M. Abolfath-Beygi, C. He, X. Li, K. L. Wong, P. Nordeen, H. Wu, G. P. Carman, X. Han, *et al.*, “Strain-induced modulation of perpendicular magnetic anisotropy in ta/cofeb/mgo structures investigated by ferromagnetic resonance,” *Applied Physics Letters*, vol. 106, no. 7, p. 072402, 2015.
- [27] W. Echtenkamp and C. Binek, “Electric control of exchange bias training,” *Physical review letters*, vol. 111, no. 18, p. 187204, 2013.
- [28] S. Emori, U. Bauer, S. Woo, and G. S. Beach, “Large voltage-induced modification of spin-orbit torques in pt/co/gdox,” *Applied Physics Letters*, vol. 105, no. 22, p. 222401, 2014.

- [29] K. Shimamura, D. Chiba, S. Ono, S. Fukami, N. Ishiwata, M. Kawaguchi, K. Kobayashi, and T. Ono, “Electrical control of curie temperature in cobalt using an ionic liquid film,” *Applied Physics Letters*, vol. 100, no. 12, p. 122402, 2012.
- [30] C. Wang, H. Zhang, C. Li, Y. He, L. Zhang, X. Zhao, Q. Yang, D. Xian, Q. Mao, B. Peng, *et al.*, “Voltage control of magnetic anisotropy through ionic gel gating for flexible spintronics,” *ACS applied materials & interfaces*, vol. 10, no. 35, pp. 29750–29756, 2018.
- [31] F. Shi, “Introductory chapter: basic theory of magnetron sputtering,” in *Magnetron Sputtering*, IntechOpen, 2018.
- [32] M. Freiser, “A survey of magnetooptic effects,” *IEEE Transactions on magnetics*, vol. 4, no. 2, pp. 152–161, 1968.
- [33] P. Garcia, A. Meinhaldt, and A. Suna, “Perpendicular magnetic anisotropy in pd/co thin film layered structures,” *Applied Physics Letters*, vol. 47, no. 2, pp. 178–180, 1985.
- [34] J. Jaworowicz, A. Maziewski, P. Mazalski, M. Kisielewski, I. Sveklo, M. Tekielak, V. Zablotskii, J. Ferré, N. Vernier, A. Mougin, *et al.*, “Spin reorientation transitions in pt/co/pt films under low dose ga+ ion irradiation,” *Applied Physics Letters*, vol. 95, no. 2, p. 022502, 2009.
- [35] R. One, S. Mican, A. Mesaros, M. Gabor, T. Petrisor, M. Joldos, L. Budă-Prejbeanu, and C. Tiusan, “Perpendicular magnetic anisotropy electric field modulation in magnetron-sputtered pt/co/x/mgo ultrathin structures with chemically tailored top interface,” *IEEE Transactions on Magnetics*, vol. 57, no. 6, pp. 1–10, 2021.

---

*REFERENCES*

- [36] O. P. Das and S. K. Pandey, “Optical, compositional and electrical properties of transparent mgo thin film for reram devices,” in *Journal of Physics: Conference Series*, vol. 2426, p. 012031, IOP Publishing, 2023.